

BEST AVAILABLE COPY



PATENT APPLICATION

IN THE UNITED STATES PATENT AND TRADEMARK OFFICE

In re application of

Docket No: Q79015

Jerry PELLETIER, et al.

Appln. No.: 10/025,222

Group Art Unit: 1656

Confirmation No.: 4998

Examiner: D.J. Steadman

Filed: December 19, 2001

For: **FRAGMENTS AND VARIANTS OF STAPHYLOCOCCUS AUREUS DNAG
PRIMASE, AND USES THEREOF**

SUBMISSION OF EXECUTED DECLARATION UNDER 37 C.F.R. §1.132

Mail Stop Amendment
Commissioner for Patents
P.O. Box 1450
Alexandria, VA 22313-1450

Sir:

Submitted herewith is a copy of an executed Declaration Under 37 C.F.R. §1.132 signed
by Greg Moeck.

Respectfully submitted,

Drew Hissong
Registration No. 44,765

SUGHRUE MION, PLLC
Telephone: (202) 293-7060
Facsimile: (202) 293-7860

WASHINGTON OFFICE

23373

CUSTOMER NUMBER

Date: June 20, 2006



PATENT APPLICATION

IN THE UNITED STATES PATENT AND TRADEMARK OFFICE

In re application of

Docket No: Q79015

Jerry PELLETIER, et al.

Appln. No.: 10/025,222

Group Art Unit: 1656

Confirmation No.: 4998

Examiner: D.J. Steadman

Filed: December 19, 2001

For: FRAGMENTS AND VARIANTS OF STAPHYLOCOCCUS AUREUS DNAG
PRIMASE, AND USES THEREOF

DECLARATION UNDER 37 C.F.R. § 1.132

Mail Stop Amendment
Commissioner for Patents
P.O. Box 1450
Alexandria, VA 22313-1450

Sir:

I, Greg Mocck, hereby declare and state:

THAT I am a citizen of Canada;

THAT I have received the degree of Ph.D. in 1997 from McGill University;

THAT I have been employed by Targanta Therapeutics since January 4, 2000, where I
hold a position as Director, Biology, with responsibility for discovery and preclinical
development of antibiotic candidates;

I have reviewed the Office Action dated March 24, 2006, issued in the above-identified
U.S. patent application. In particular, I have reviewed and understand the rejection of claim 72
as being anticipated under 35 U.S.C. §102(b) by O'Donnell et al. (WO 99/37661).

In particular, I understand that the Examiner has stated that O'Donnell teaches a
polypeptide that has a carboxy-terminal sequence (amino acids 534-572) that is 100% identical

to SEQ ID NO:6, where SEQ ID NO:6 is the sequence of the first polypeptide recited in claim 72. The Examiner further states that while O'Donnell fails to teach whether the disclosed polypeptide binds SEQ ID NO:4 (the second polypeptide of claim 72), because the present specification teaches that a polypeptide having SEQ ID NO:6 at the carboxy-terminus binds to SEQ ID NO:4, in the absence of evidence to the contrary the polypeptide of O'Donnell would be expected to bind SEQ ID NO:4.

While O'Donnell may indeed teach a polypeptide that has carboxyl-terminal sequence that is 100% identical to SEQ ID NO:6 of claim 72, the skilled artisan would not readily expect the O'Donnell polypeptide to bind to the polypeptide of SEQ ID NO:4.


There are examples in the literature of 'auto-inhibition' in which juxtaposition of regulatory and functional domains within the same polypeptide results in repression of the activity of the functional domain of the polypeptide (*see, e.g.,* Prehoda et al. *Science* 290:801-806 (2000), and Sondermann et al. *Cell* 119:393-405 (2004), both of which are enclosed). In other words, it is well-understood that there are a number of polypeptides having domains within the same protein that structurally interact with one another to regulate the protein's activity. In Prehoda, N-WASP was shown inhibit its own activity via contact between its N-terminal GTPase binding domain and its C-terminal cofilin homology domain. In Sondermann, the allosteric Ras-binding site on the SOS protein was shown to be auto-inhibited by the Dbl-pleckstrin homology domains of SOS. The O'Donnell polypeptide could contain such interacting domains, whereby the carboxy-terminus of the O'Donnell polypeptide is blocked from binding to other polypeptides.

DECLARATION UNDER 37 C.F.R. § 1.132
U.S. Appln. No. 10/025,222

Q79015

I declare further that all statements made herein of my own knowledge are true and that all statements made on information and belief are believed to be true; and further that these statements were made with the knowledge that willful false statements and the like so made are punishable by fine or imprisonment, or both, under Section 1001 of Title 18 of the United States Code, and that such willful false statements may jeopardize the validity of the application or any patent issuing thereon.

Date: June 20, 2006



Greg Moeck

REPORTS

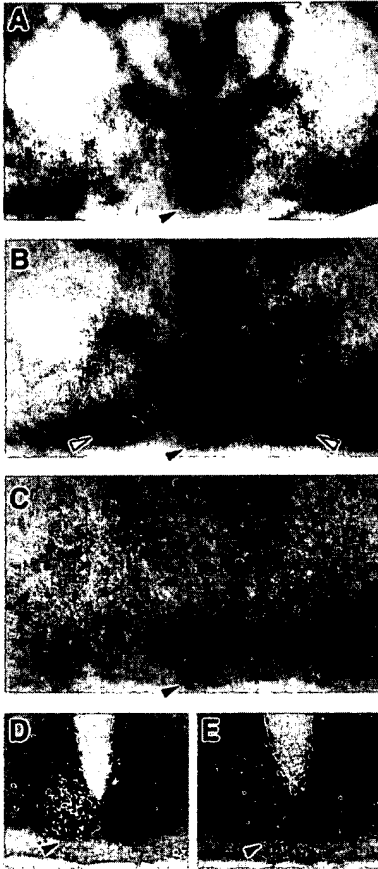


Fig. 3. SCN AVP and *c-fos* gene expression in the behaviorally split hamster. Coronal brain sections through the SCN were processed for in situ hybridization. SCN AVP mRNA levels were relatively high [black arrowhead in (B)] on the side of the SCN ipsilateral to high *Per1* expression [arrowhead in (A)]; AVP levels in the supraoptic nuclei were symmetrical [open arrowheads in (B)]; black dots in the autoradiograph are small clusters of magnocellular AVP perikarya. SCN *c-fos* mRNA levels were relatively high [arrowhead in (C)] on the same side as *Per1* and AVP, and immunohistochemistry for the *c-Fos* protein showed a unilateral rostral [arrowhead in (D)] and dorsal [arrowhead in (E)] distribution. Scale bars: 1.1 mm, (A) to (C); 400 μ m, (D) and (E).

and right-sided circadian oscillators. This is a unique neural state, a "split" brain without surgical bisection. Because AVP is a neurotransmitter controlled by the SCN clock, and because AVP and other SCN efferents project ipsilaterally to their targets (37), other bilaterally represented brain regions outside the SCN may also be running on antipodal time.

References and Notes

1. D. C. Klein, R. Y. Moore, S. M. Reppert, Eds., *Suprachiasmatic Nucleus: The Mind's Clock* (Oxford Univ. Press, New York, 1991).
2. D. K. Welsh, D. E. Logothetis, M. Meister, S. M. Reppert, *Neuron* **14**, 697 (1995).
3. D. P. King, J. S. Takahashi, *Annu. Rev. Neurosci.* **23**, 713 (2000).
4. C. S. Pittendrigh, S. Daan, *J. Comp. Physiol. A* **106**, 333 (1976).

5. C. A. Shibuya, R. B. Melnyk, N. Mrosovsky, *Naturwissenschaften* **67**, 45 (1980).
6. G. E. Pickard, R. Kahn, R. Silver, *Physiol. Behav.* **32**, 763 (1984).
7. J. M. Swann, F. W. Turek, *Science* **228**, 898 (1985).
8. P. Zlomaniczuk, R. R. Margraf, G. R. Lynch, *Brain Res.* **559**, 94 (1991).
9. S. Daan, C. Berde, *J. Theor. Biol.* **70**, 297 (1978).
10. J. C. Lees, J. D. Hallonquist, N. Mrosovsky, *J. Comp. Physiol. A* **153**, 123 (1983).
11. Z. Boulos, L. P. Morin, *J. Biol. Rhythms* **1**, 1 (1986).
12. J. H. Meijer, S. Daan, G. J. F. Overkamp, P. M. Hermann, *J. Biol. Rhythms* **5**, 1 (1990).
13. G. E. Pickard, F. W. Turek, *Science* **215**, 1119 (1982).
14. M. E. Harrington, G. A. Eskes, P. Dickson, B. Rusak, *Brain Res. Bull.* **24**, 593 (1990).
15. M. Akiyama et al., *J. Neurosci.* **19**, 1115 (1999).
16. B. Zheng et al., *Nature* **400**, 169 (1999).
17. Linearized recombinant plasmids were used as templates for the generation of antisense cRNA probes: hamster *Per1* [783-base pair (bp) cDNA insert in Bluescript II SK+], hamster *Per2* (791-bp insert in pGEM-T Easy), hamster *Per3* (819-bp insert in pGEM-T Easy), hamster *Bmal1* (2.4-kb insert in pVP16), rat *c-fos* (2.3-kb insert in pSP65), and rat AVP (241-bp insert in pGEM3). Probes were transcribed in the presence of [³⁵S]uridine triphosphate with the appropriate RNA polymerases with the Maxiscript kit (Ambion). Hamsters were decapitated, brains were rapidly removed and frozen, and in situ hybridization was performed on 15- μ m-thick coronal sections as previously described (38).
18. U. Albrecht, Z. S. Sun, G. Eichele, C. C. Lee, *Cell* **91**, 1055 (1997).
19. T. Takumi et al., *EMBO J.* **17**, 4753 (1998).
20. E. S. Maywood, N. Mrosovsky, M. D. Field, M. H. Hastings, *Proc. Natl. Acad. Sci. U.S.A.* **96**, 15211 (1999).
21. S. Honma et al., *Biochem. Biophys. Res. Commun.* **250**, 83 (1998).
22. L. P. Shearman et al., *Science* **288**, 1013 (2000).
23. X. Jin et al., *Cell* **96**, 57 (1999).
24. S. M. Reppert, W. J. Schwartz, G. R. Uhl, *Trends Neurosci.* **10**, 76 (1987).
25. I. Chambille, S. Doyle, J. Servière, *Brain Res.* **612**, 138 (1993).
26. M. E. Guido, D. Goguen, L. De Guido, H. A. Robertson, B. Rusak, *Neuroscience* **90**, 555 (1999).
27. Hamsters were deeply anesthetized with pentobarbital (20 mg per 100 g of body weight, intraperitoneal) and perfused with 25 ml of heparinized 0.01 M phosphate-buffered saline followed by 100 ml of cold 4% paraformaldehyde in 0.1 M phosphate buffer. Brains were postfixed overnight at 4°C, and 40- μ m-thick sections were incubated with antiserum to *c-Fos*₃₋₁₇ (1:10,000; SC52; Santa Cruz Biotechnology) for 48 hours at 4°C and processed for immunohistochemistry as described (38).
28. D. J. Hudson, M. E. Lickey, *Brain Res.* **183**, 481 (1980).
29. W. K. Koehler, G. Fleissner, *Nature* **274**, 708 (1978).
30. T. L. Page, *J. Comp. Physiol. A* **124**, 225 (1978).
31. G. Wiedenmann, *J. Comp. Physiol. A* **150**, 51 (1983).
32. J. D. Palmer, *Bioessays* **22**, 32 (2000).
33. A. Sumová, H. Illnerová, *Am. J. Physiol.* **274**, R857 (1998).
34. A. Jagota, H. O. de la Iglesia, W. J. Schwartz, *Nature Neurosci.* **3**, 372 (2000).
35. F. C. Davis, R. A. Gorski, *J. Comp. Physiol. A* **154**, 221 (1984).
36. F. C. Davis, N. Viswanathan, *J. Biol. Rhythms* **11**, 291 (1996).
37. A. Kalsbeek, R. Teclemariam-Mesbah, P. Pévet, *J. Comp. Neurol.* **332**, 293 (1993).
38. W. J. Schwartz et al., *Neuroscience* **98**, 535 (2000).
39. We thank T. Curran, H. Okamura, S. Shibata, T. Sherman, and C. Weitz for gifts of recombinant plasmids. Supported by R01 NS24542 (to W.J.S.).

27 June 2000; accepted 13 September 2000

Integration of Multiple Signals Through Cooperative Regulation of the N-WASP-Arp2/3 Complex

Kenneth E. Prehoda,^{1,2} Jessica A. Scott,^{1,2} R. Dyche Mullins,¹ Wendell A. Lim^{1,2*}

The protein N-WASP [a homolog to the Wiskott-Aldrich syndrome protein (WASP)] regulates actin polymerization by stimulating the actin-nucleating activity of the actin-related protein 2/3 (Arp2/3) complex. N-WASP is tightly regulated by multiple signals: Only costimulation by Cdc42 and phosphatidylinositol (4,5)-bisphosphate (PIP₂) yields potent polymerization. We found that regulation requires N-WASP's constitutively active output domain (VCA) and two regulatory domains: a Cdc42-binding domain and a previously undescribed PIP₂-binding domain. In the absence of stimuli, the regulatory modules together hold the VCA-Arp2/3 complex in an inactive "closed" conformation. In this state, both the Cdc42- and PIP₂-binding sites are masked. Binding of either input destabilizes the closed state and enhances binding of the other input. This cooperative activation mechanism shows how combinations of simple binding domains can be used to integrate and amplify coincident signals.

Many cellular processes are controlled by networks of interacting signaling pathways (1, 2). For example, during directed cell motility, multiple pathways converge to precisely target actin polymerization to the cell's

leading edge. Little is known, however, about the molecular mechanisms by which the relevant signaling proteins integrate these multiple inputs to yield a coordinated response.

WASP and its homolog N-WASP link

multiple signaling pathways to actin assembly (3–5). N-WASP interacts with the Arp2/3 complex and activates its ability to nucleate actin filaments (5, 6). Activation only occurs, however, when N-WASP is stimulated by the proper set of upstream signals. The two best characterized inputs are the rho family guanosine triphosphatase (GTPase) Cdc42 and phosphatidylinositol 4,5-bisphosphate (PIP₂), both of which are regulated by upstream pathways critical for motility (1, 7, 8). Individually, Cdc42 and PIP₂ are weak activators of N-WASP. Together, however, the inputs act synergistically: costimulation with low concentrations of both yields potent activation (5). Thus, N-WASP acts as a signal integration device that can precisely target actin polymerization to sites on the membrane at which both PIP₂ and activated Cdc42 are present.

Several domains within N-WASP have been implicated in this signal processing behavior (Fig. 1A). Output is controlled by a COOH-terminal domain that directly interacts with and activates the Arp2/3 complex

(5). This domain is referred to as the VCA domain (also called WWA) because it has a verprolin homology motif (V), a cofilin homology motif (C), and an acidic motif (A). The acidic motif binds Arp2/3, whereas the verprolin motif binds actin monomers, probably delivering them to Arp2/3 (5, 6). The isolated VCA domain is constitutively active; however, this activity is suppressed in full-length N-WASP, indicating that NH₂-terminal regions play a regulatory role (5). One key regulatory domain is the GTPase-binding domain (GBD), which forms an intramolecular interaction with the cofilin homology motif (Fig. 1A) (9, 10). Because activated Cdc42 can disrupt the intramolecular interaction by binding the GBD, a simple model for N-WASP regulation has been proposed: the intramolecular interaction between the GBD and the cofilin motif blocks binding of Arp2/3 to the VCA domain, and Cdc42 relieves this autoinhibitory interaction (3, 5, 9). There are several problems with this model. First, the GBD has never experimentally been shown to block Arp2/3 binding or to suffice as a functional repressor of the VCA domain. Second, this simple autoinhibition model fails to explain how PIP₂ is detected as an input, and how its effects are synergistically integrated with those of Cdc42.

To elucidate the mechanism of N-WASP regulation and signal integration, we identified

the minimal domains required to repress the VCA domain, mapped their interactions, and determined how they communicate. We found that two adjacent regulatory domains, the GBD and a novel PIP₂-binding motif, are necessary and sufficient for proper repression and regulation of N-WASP. In the absence of stimuli, the two regulatory motifs together lock the VCA-Arp2/3 complex in an inactive “closed” conformation. The mechanism of repression allows for highly cooperative activation: Cdc42 and PIP₂ disrupt the closed state in a thermodynamically coupled fashion, providing the basis for potent signal integration by N-WASP.

VCA domain activity was potently repressed (inhibition constant $K_i = \sim 1 \mu\text{M}$) by a minimal fragment containing both the GBD and an adjacent, highly basic motif in an *in vitro* actin polymerization assay (Fig. 1B). We refer to this composite domain as the “control region.” The basic motif is only ~20 residues in length and contains nine lysine residues (11). In contrast, a second fragment consisting solely of the GBD, although able to interact strongly with the VCA domain, had virtually no inhibitory effect (Fig. 1B), even at concentrations (100 μM) well above saturation (12). The GBD failed to inhibit even when covalently tethered (*cis*) to the VCA domain (13). A third fragment that contains the basic motif and only half of the GBD was also unable to repress (Fig. 1B). These data show that current models for autoinhibition are incorrect: although required, the GBD alone is insufficient to repress VCA activation of the Arp2/3 complex; rather, the composite control region is the minimal repressive element.

Remarkably a “mini-N-WASP” that contains only the control region and the VCA domain attached by a nine-residue linker is also sufficient to recapitulate the hallmark regulatory behavior of N-WASP. Its Arp2/3 stimulatory activity is highly repressed but can be synergistically activated by costimulation with PIP₂ and Cdc42 complexed with guanosine 5'-O-(3'-thiotriphosphate) (Cdc42-GTP γ S) (Fig. 1C) (14).

Contrary to previous models, we found that neither the control region nor GBD blocks binding of Arp2/3 to the VCA domain (Fig. 2A) (15). Instead, the basic motif participates in two previously uncharacterized interactions critical for regulation (Fig. 2, B through D). First, the basic motif is an essential part of a novel Arp2/3 binding site (Fig. 2B). Although this Arp2/3 interaction region appears to be crucial for repression, it is not sufficient, because a fragment that binds Arp2/3 but lacks the intact GBD (residues 178 through 244) also fails to inhibit VCA activity (Fig. 1B). Arp2/3 therefore interacts with two sites within N-WASP: the acidic motif within the VCA domain and the basic motif within the control region. Second, we found that the basic region is also a novel

¹Department of Cellular and Molecular Pharmacology, and ²Department of Biochemistry and Biophysics, University of California, San Francisco, CA 94143–0450, USA.

*To whom correspondence should be addressed. E-mail: wlim@itsa.ucsf.edu

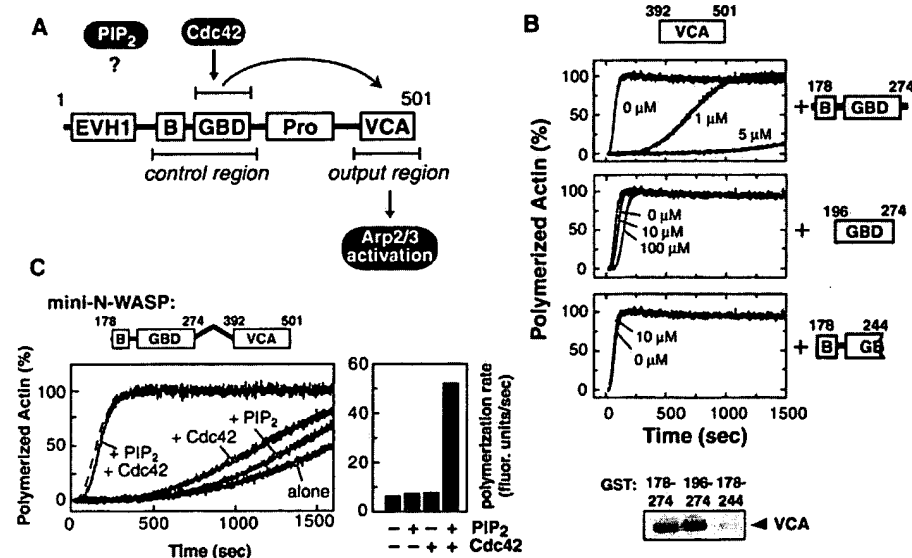


Fig. 1. Both the basic motif and GBD are required for repression and regulation of N-WASP. (A) N-WASP contains the following domains: EVH1 domain, basic motif (B), GBD, proline-rich motif (Pro), and verprolin/cofilin/acidic domain (VCA). Curved arrow indicates intramolecular interaction between GBD and the cofilin motif (within the VCA domain) (9, 10). (B) Repression of VCA-Arp2/3-mediated actin polymerization by control region fragments (25), tested using *in vitro* pyrene actin polymerization assay (26). Assays contain 50 nM VCA, 50 nM Arp2/3, and 2.5 μM actin (2% pyrene actin), along with the indicated concentration of variable fragment. Binding of the VCA domain to these control region fragments fused to GST (27) is shown below. (C) Mini-N-WASP (178–274–GSGSGSGSG–392–501) mimics the regulatory behavior of N-WASP (28). Pyrene actin polymerization assays are shown for mini-N-WASP alone and mini-N-WASP plus Cdc42-GTP γ S (0.15 μM), PIP₂ (~0.4 μM in PS:PC:PIP₂ vesicles at 48:48:2), or both (same concentrations as above). Activity of VCA domain alone (dotted line) is shown for comparison. Assays contain 50 nM mini-N-WASP, 50 nM Arp2/3, and 2.5 μM actin. Bar graph shows maximal polymerization rate for each assay.

REPORTS

phospholipid-binding module that specifically recognizes PIP_2 (Fig. 2C). This 20-residue motif is distinct from larger canonical phospholipid-binding domains, such as pleckstrin homology (16) or FYVE finger domains (17).

The interactions of the control region (Fig. 2D) and the requirements for repression (Fig. 1B) support a concerted repression model. Neither the GBD nor the basic motif is intrinsically repressive; rather, each alone is a neutral anchor point that, only when topologically linked to and acting in concert with the other, locks the N-WASP-Arp2/3 complex in an inactive "closed" state (Fig. 2D). These interactions may alter the conformation of Arp2/3 and/or its relationship with the VCA domain, rendering it inactive. This model is supported by the finding that when the GBD and basic modules are added together, but as covalently distinct elements, they fail to repress VCA domain activity (13).

Moreover, these control region subfragments are found to activate mini-N-WASP (Fig. 2E), behavior incompatible with subfragments that are intrinsically repressive (these would repress or be neutral). The behavior is best explained as uncoupling of concerted interactions required for repression (Fig. 2E).

The novel mechanism of N-WASP repression suggests a reciprocal mechanism for activation by both Cdc42 and PIP_2 . These inputs bind the GBD and basic motifs, respectively, and thus either could disrupt the "closed" state and release the active VCA-Arp2/3 complex. Activated Cdc42 is known to disrupt the intramolecular GBD-VCA interaction (9, 10). We find that Cdc42 also disrupts the control region-Arp2/3 interaction (Fig. 3A). However, this alone cannot explain synergistic activation by PIP_2 and Cdc42.

Synergistic activation could be explained, however, if PIP_2 and Cdc42 act cooperatively to disrupt the closed state. Therefore, we

tested if binding of the two inputs is thermodynamically coupled. Vesicle-binding studies show that PIP_2 and Cdc42 can bind the control region simultaneously (Fig. 3B), and that in the context of mini-N-WASP, Cdc42 can dramatically enhance PIP_2 binding (Fig. 3C). Moreover, parallel fluorescence binding studies show that PIP_2 can enhance Cdc42 binding to the control region, in the presence of Arp2/3 (Fig. 3D). Thus, cooperative binding of PIP_2 and Cdc42 to N-WASP has been observed.

However, this observed cooperativity discussed above cannot result from direct interaction between Cdc42 and PIP_2 , because the two inputs do not bind cooperatively to the isolated control region (Fig. 3, C and D). Instead, cooperativity must result from coordinated competition with other control region (B-GBD) ligands. For example, interaction of the control region with the VCA domain, present in mini-N-WASP, appears to mask both the PIP_2 - and

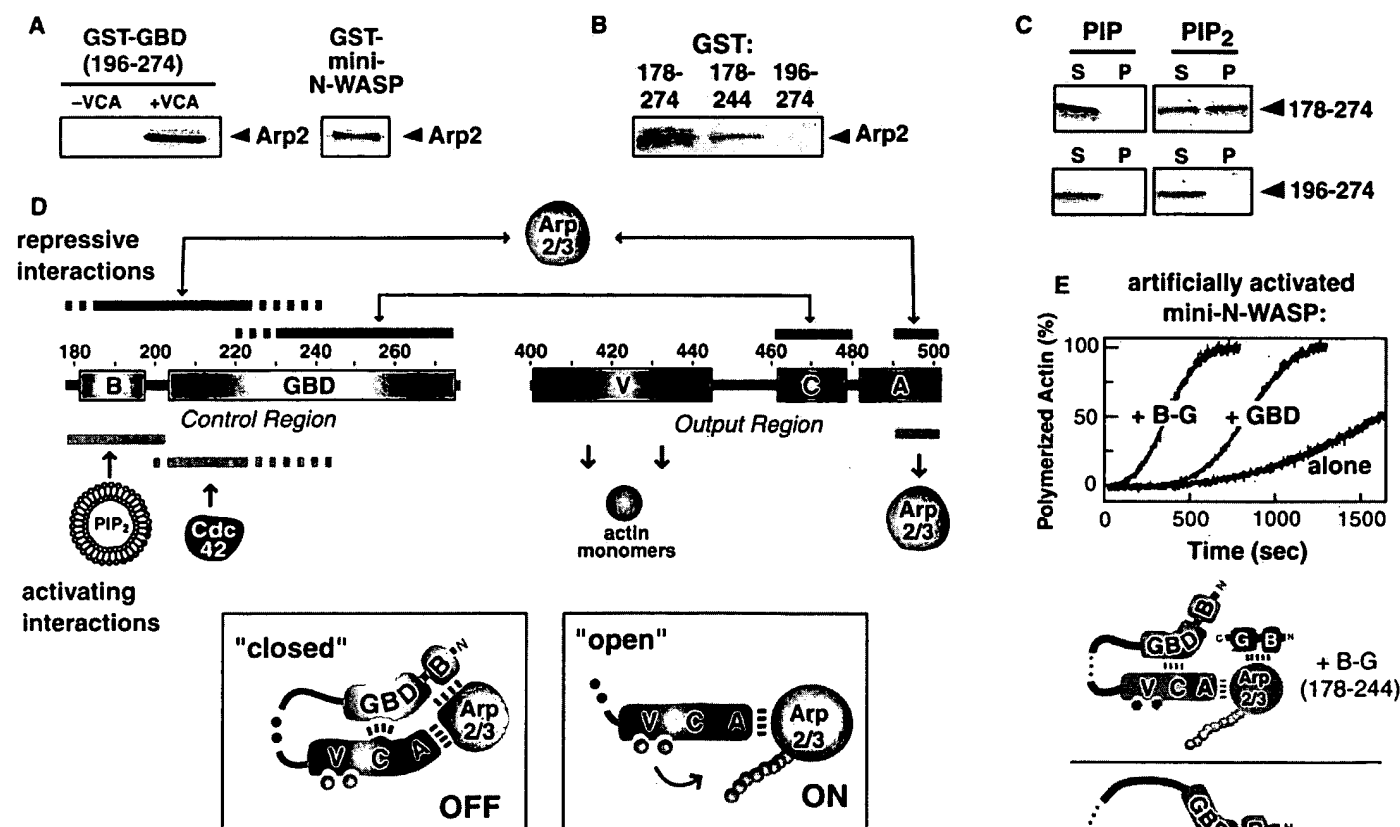


Fig. 2. Repression of the N-WASP-Arp2/3 complex requires a network of concerted interactions. (A) Arp2/3 binding to the VCA domain is not blocked by the GBD (residues 196–274) or control region (178–274). Arp2/3 (1 μM) can bind to VCA (10 μM) precomplexed with a GST-GBD fusion (27). Arp2/3 can also bind GST-mini-N-WASP, which contains the full control region and is repressed. (B) Direct binding of Arp2/3 to GST fusions of control region fragments (27). (C) PIP and PIP_2 vesicle spin-down binding assays (29). S indicates supernatant (unbound) and P indicates pellet (bound). Control region (residues 178–274) can selectively bind PIP_2 whereas the GBD alone (residues 196–274) cannot. (D) Summary of control region and output region interactions mapped in this study [complete supplementary data is given in Web fig. 1 (30)]. Solid lines are essential regions; dotted lines are important but nonessential regions. Also shown is a cartoon of the repressed, "closed" state of the N-WASP-Arp2/3 complex (31). The interactions in the closed state could repress by inducing a conformational change in Arp2/3 and/or the VCA domain, or a change in the arrangement of the two components. Disruption of these interactions allows conversion to the active, "open" state. (E) Artificial disruption of the repressive network leads to activation. Control region subfragments consisting of either the GBD alone, or the basic motif with a truncated GBD (+B-G), activate mini-N-WASP. Actin polymerization assays were performed with 80 nM mini-N-WASP \pm 10 μM of either subfragment. The postulated mechanism of artificial activation is shown.

REPORTS

Fig. 3. Cdc42 and PIP₂ bind cooperatively to N-WASP when competing against repressive interactions. (A) Cdc42-GTPγS inhibits Arp2/3 binding to a GST-control region fragment (27). (B) PIP₂ vesicle binding assays (29) show that Cdc42-GTPγS and PIP₂ can simultaneously bind the control region (B-GBD). S indicates supernatant (unbound) and P indicates pellet (bound). Cdc42-GTPγS does not bind to PIP₂ vesicles in the absence of the control region (not shown). (C) Cdc42-GTPγS enhances mini-N-WASP binding to PIP₂. In the absence of Cdc42, mini-N-WASP binds poorly to PIP₂, most likely because the GBD-VCA interaction sterically masks the PIP₂-binding site. High-affinity PIP₂ binding is observed if Cdc42 is present, or if the VCA domain is removed. The cooperative effects between Cdc42 and PIP₂ are not observed for binding to the control region alone (B-GBD). (D) PIP₂ enhances apparent affinity of Cdc42 for the control region-Arp2/3 complex. Dissociation constants for the control region interaction with fluorescently tagged Cdc42 (32), either alone (K_d) or with additional factors (K_d^{app}), were measured as described in Web fig. 2 (30). We added 2.5 μM of Arp2/3 or 10 μM of PIP₂ (PC:PS:PIP₂ at ratios of 48:48:2), or both. The presence of Arp2/3 significantly decreases the apparent affinity, as expected, because Arp2/3 competes against Cdc42 for binding to the control region (A). However, addition of PIP₂ with Arp2/3 restores the higher apparent affinity, indicating that PIP₂ and Cdc42 cooperate to compete against Arp2/3 binding. Cooperation is not observed in the absence of Arp2/3.

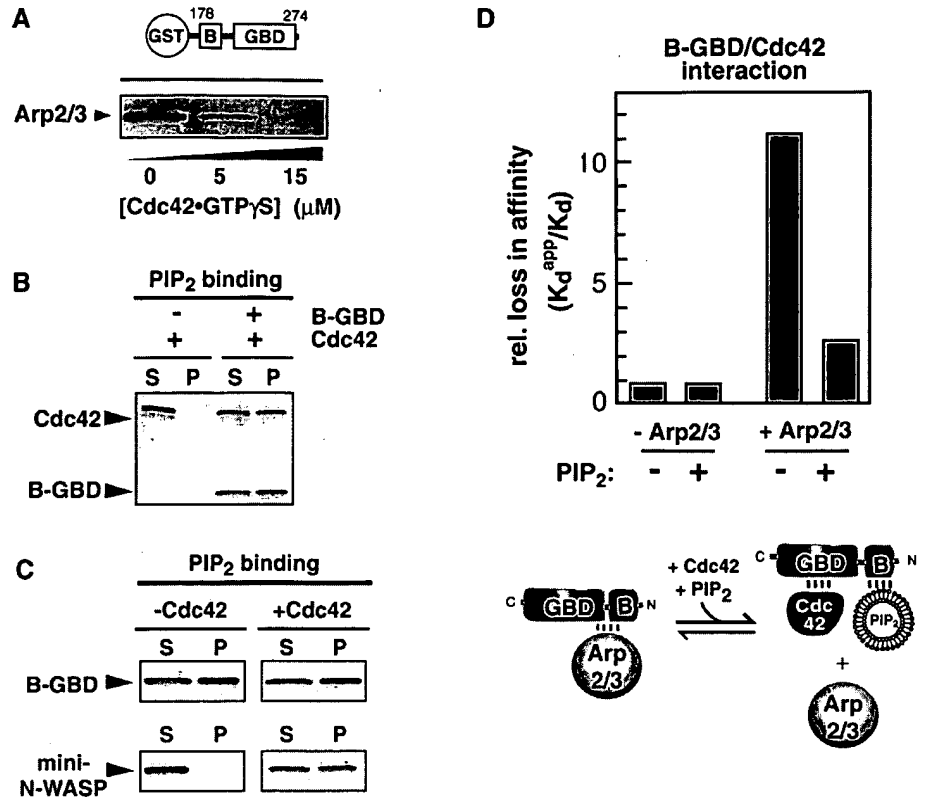
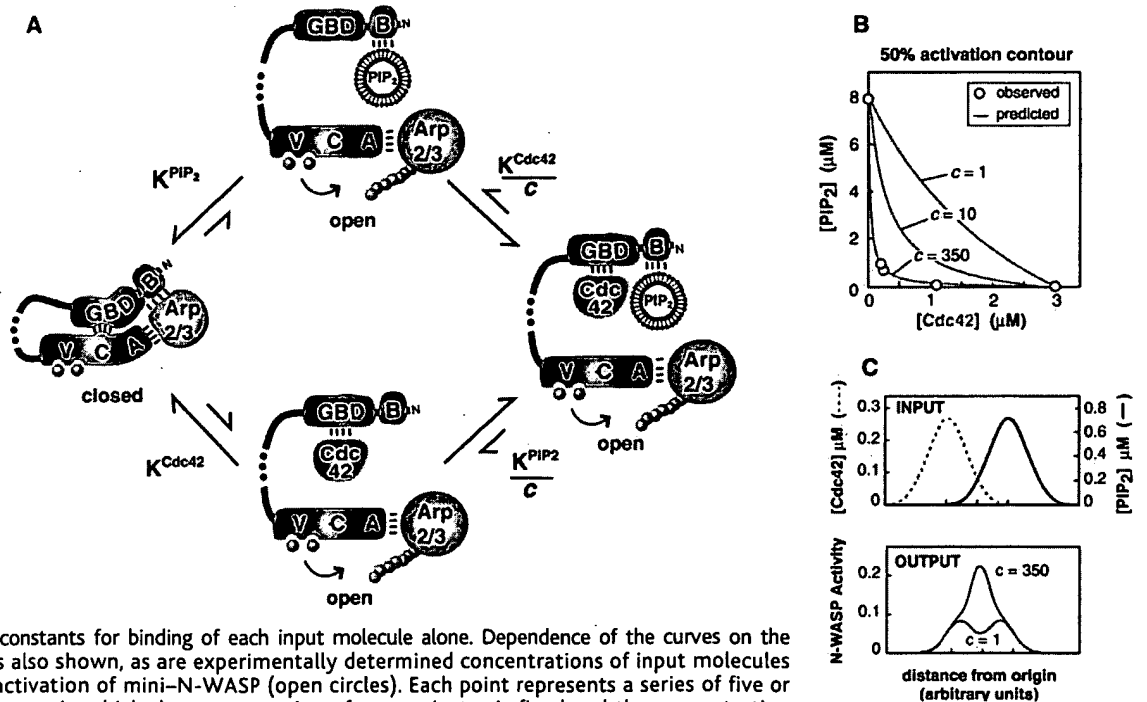


Fig. 4. Highly cooperative activation mechanism of N-WASP allows for potent signal integration. (A) Thermodynamic cycle modeling states of Cdc42 (green) and PIP₂ (purple) binding to mini-N-WASP. Binding of a second input molecule is more favorable, because the energetic cost of disrupting the closed state is paid by binding of the first input molecule. The degree of enhancement in binding is given by the cooperativity factor, c . (B) Theoretical curves indicate the concentration of two input molecules required to achieve 50% activation of a protein switch such as that modeled in (A) (33). Intercepts give the dissociation constants for binding of each input molecule alone. Dependence of the curves on the cooperativity constant, c , is also shown, as are experimentally determined concentrations of input molecules required to achieve 50% activation of mini-N-WASP (open circles). Each point represents a series of five or six actin polymerization assays in which the concentration of one activator is fixed and the concentration of the second activator is varied [Web fig. 3 (30)]. The 50% activation points (K_{act}) are determined based on maximal rates of actin polymerization. Data fit the model with $c \sim 350$. (C) Cooperativity provides a mechanism for signal integration. Top graph shows hypothetical, spatially overlapping concentration gradients of Cdc42-GTP (green) and PIP₂ (purple). The bottom graph shows the calculated response of N-WASP (fraction maximal activity) assuming the model in (A) and a cooperativity of either 1 or 350. With high cooperativity, coincident signals are integrated and amplified.



Cdc42-binding sites (Fig. 3C). Thus, Cdc42 strongly enhances PIP₂ binding in this context. Arp2/3 binding to the control region also ap-

pears to mask both the Cdc42- and PIP₂-binding sites, explaining the cooperative effects of the two inputs in this context (Fig. 3D). In

summary, it is the structure and interactions within the closed state that makes binding of the two inputs highly cooperative.

The activation behavior of N-WASP can thus be modeled, using the thermodynamic cycle shown in Fig. 4A. In the repressed state, a network of interactions holds the N-WASP-Arp2/3 complex in a closed state. Cdc42 and PIP₂ can individually disrupt this network and activate the complex. However, because their binding sites are masked by repressive interactions, binding of either input alone to the closed state is relatively weak. In contrast, if one input molecule is prebound, the closed state is destabilized, and binding of the second molecule is considerably enhanced. The degree to which binding of one ligand enhances binding of the other is determined by the cooperativity factor, c . This behavior is analogous to that of any cooperative binding protein, such as hemoglobin (18, 19), although in this case, cooperativity is observed between heterotropic rather than homotropic ligands. Nonetheless, both mechanisms involve increasing stabilization of an open or relaxed state by binding of successive ligands.

This framework reveals that a highly cooperative activation mechanism allows for potent signal integration. A series of simulated contours indicating the concentrations of two activating inputs required to achieve 50% activation is shown in Fig. 4B. If two input ligands are completely independent ($c = 1$), their combined effects are nearly additive and the 50% activation contour will be close to linear. In contrast, if c is high, the two ligands will act synergistically. The 50% activation contour will be concave, because when added together, significantly lower concentrations of each ligand are required for activation.

We experimentally measured activation of mini-N-WASP as a function of both Cdc42 and PIP₂ concentration (Fig. 4B). High concentrations of either input alone ($\sim 3 \mu\text{M}$ Cdc42 or $\sim 8 \mu\text{M}$ PIP₂) are required to yield 50% activation. However, costimulation with 10-fold less of each input yields the same degree of activation. The observed behavior closely fits that predicted by our model with a cooperativity factor of >100 linking Cdc42 and PIP₂ activation (20).

These results indicate that N-WASP can exist in a primed state that, although repressed, is preloaded with Arp2/3 and ready for immediate actin filament assembly upon activation (21). The high cooperativity by which this state of N-WASP is activated allows it to detect and amplify weak but coincident signals of both Cdc42 and PIP₂ (Fig. 4C) (22). Thus, N-WASP approximates a coincidence detector or a logical "AND" gate, devices whose output is dependent on stimulation by the proper combination of inputs (23). The mechanism of N-WASP regulation reveals general principles by which simple protein interaction modules, if combined in the proper

cooperative fashion, can yield a sophisticated signal-integrating machine.

Note added in proof: Rohatgi *et al.* (34) have recently also identified the basic motif of N-WASP as the PIP₂ responsive element.

References and Notes

1. C. A. Parent, P. N. Devreotes, *Science* **284**, 765 (1999).
2. T. J. Mitchison, L. P. Cramer, *Cell* **84**, 371 (1996).
3. M. F. Carlier, A. Ducruix, D. Pantaloni, *Chem. Biol.* **6**, R235 (1999).
4. R. D. Mullins, *Curr. Opin. Cell Biol.* **12**, 91 (2000).
5. R. Rohatgi *et al.*, *Cell* **97**, 221 (1999).
6. L. M. Machesky, R. H. Insall, *Curr. Biol.* **8**, 1347 (1998).
7. M. P. Czech, *Cell* **100**, 603 (2000).
8. A. Hall, *Science* **279**, 509 (1998).
9. A. S. Kim, L. T. Kakalis, N. Abdul-Manan, G. A. Liu, M. K. Rosen, *Nature* **404**, 151 (2000).
10. H. Miki, T. Sasaki, Y. Takai, T. Takenawa, *Nature* **391**, 93 (1998).
11. The specific sequence of the basic motif [NHSIT-KEKKKGAKKKRLTK (24)] is essential for repression; mutation of nine lysines to alanine abolishes repression (K. E. Prehoda, W. A. Lim, data not shown).
12. The measured affinity for the WASP GBD-VCA interaction is $K_d \sim 1 \mu\text{M}$ (9).
13. K. E. Prehoda, W. A. Lim, data not shown.
14. Like full-length N-WASP, the degree of mini-N-WASP activation is dependent on the nucleotide state of Cdc42 (5). Our findings with mini-N-WASP show that the enabled/VASP homology 1 (EVH1) domain and proline-rich region are unnecessary for this mode of regulation. These other domains may be involved in targeting [V. Moreau *et al.*, *Nature Cell Biol.* **2**, 441 (2000)] or in modes of regulation distinct from that mediated by the control region. Our findings contradict previous suggestions that the EVH1 domain is the input point for PIP₂ activation (5) [H. Miki, K. Miura, T. Takenawa, *EMBO J.* **15**, 5326 (1996); K. E. Prehoda, D. J. Lee, W. A. Lim, *Cell* **97**, 471 (1999)]. We found that the N-WASP EVH1 domain is a peptide-binding module and does not bind acidic phospholipids (K. E. Prehoda, J. A. Scott, W. A. Lim, in preparation).
15. Addition of high concentrations of the control region can apparently inhibit interaction of Arp2/3 with the VCA domain. However, interpretation of this experiment is complicated by our subsequent finding that there is a second Arp2/3-binding site in the control region (see below) which can, at stoichiometric excess, competitively deplete available Arp2/3.
16. D. A. Fruman, L. E. Rameh, L. C. Cantley, *Cell* **97**, 817 (1999).
17. H. Stenmark, R. Aasland, *J. Cell Sci.* **112**, 4175 (1999).
18. J. Monod, J. P. Changeux, F. Jacob, *J. Mol. Biol.* **6**, 306 (1963).
19. M. F. Perutz, *Sci. Am.* **239**, 92 (December 1978).
20. This value is likely to be a lower estimate for the cooperativity in vivo, since activated Cdc42 is normally prenylated [F. L. Zhang, P. J. Casey, *Annu. Rev. Biochem.* **65**, 241 (1996)]. Thus, both inputs would be restricted to the membrane, and their effective concentrations with respect to one another would be even higher.
21. These results show that exclusion of Arp2/3 is not required for repression. However, it is possible that other elements in full-length N-WASP function by blocking Arp2/3 binding.
22. This model predicts that N-WASP will have a limited range of optimal sensitivity. High concentrations of either individual input can overload the system, consistent with observations that either overexpression of a Cdc42 exchange factor [Y. Zheng *et al.*, *J. Biol. Chem.* **271**, 33169 (1996)] or phosphoinositide 5-kinase [A. Rozelle *et al.*, *Curr. Biol.* **10**, 311 (2000)] results in unregulated actin polymerization. N-WASP's signal integration properties are likely optimized for the physiologically relevant range of input concentrations, just as the oxygen-binding properties of hemoglobin are set for the observed range of oxygen partial pressure [M. Perutz, *Cooperativity and*

Allosteric Regulation in Proteins (Cambridge Univ. Press, Cambridge, 1990)].

23. H. R. Bourne, R. Nicoll, *Cell (Suppl.)* **72**, 65 (1993).
24. Single-letter abbreviations for the amino acid residues are as follows: A, Ala; C, Cys; D, Asp; E, Glu; F, Phe; G, Gly; H, His; I, Ile; K, Lys; L, Leu; M, Met; N, Asn; P, Pro; Q, Gln; R, Arg; S, Ser; T, Thr; V, Val; W, Trp; and Y, Tyr.
25. N-WASP fragments were cloned by polymerase chain reaction from a rat cDNA library. Proteins were expressed as fusions to either a polyhistidine tag or glutathione S-transferase (GST). Proteins were expressed in *Escherichia coli* (BL21-DE3) and purified by chromatography on Ni-NTA resin (Qiagen) or glutathione agarose resin (Sigma), followed by Source 5 or Q resins (Pharmacia). The polyhistidine tag was removed by incubation with tobacco etch virus (TEV) protease, except when required for detection in Western blots.
26. Actin polymerization assays were performed as described [L. M. Machesky *et al.*, *Proc. Natl. Acad. Sci. U.S.A.* **96**, 3739 (1999)]. Briefly, polymerization of actin doped with 1.2% pyrene-labeled actin was monitored via change in fluorescence (excitation: 366 nm; emission: 407 nm). Before the reaction, actin was converted from the Ca-ATP to the Mg-ATP form by adding MgCl₂ and EGTA to final concentrations of 50 and 200 μM , respectively, and incubating at 25°C for 2 min. To initiate polymerization, actin was added to a solution containing Arp2/3 and any other factors at 20°C. Final conditions were 2.5 μM total actin, 50 mM KCl, 1 mM MgCl₂, 1 mM EGTA, 10 mM imidazole (pH 7.0), 0.2 mM ATP, and 1 mM DTT in a volume of 100 μl . Arp2/3 and actin were purified from *Acanthamoeba castellanii* as described in the above reference. Rabbit skeletal muscle actin was pyrene-labeled as described [S. MacLean-Fletcher, T. D. Pollard, *Cell* **20**, 329 (1980)].
27. GST-fusion binding assays were performed by immobilizing GST-fusion proteins on glutathione agarose beads (Sigma). We incubated 5 μl of beads with the appropriate target proteins in binding buffer [20 mM HEPES (pH 7.0), 100 mM NaCl, 1 mM dithiothreitol (DTT)] in a total volume of 100 μl (final GST-fusion concentration of $\sim 10 \mu\text{M}$). After gentle rotation at 4°C for 30 min, beads were washed three times with 1 ml binding buffer plus 0.05% Tween-20. Bound proteins were analyzed by SDS-polyacrylamide gel electrophoresis (SDS-PAGE) and visualized by coomassie blue staining or by Western blotting with anti-Arp2 or anti-polyhistidine antibodies (Qiagen).
28. Human Cdc42 was expressed in *E. coli* as a fusion to GST, and activated by incubating with 100 μM GTP γ S for 30 min at room temperature, followed by addition of MgCl₂ to a 10 mM final concentration [C. Egile *et al.*, *J. Cell Biol.* **146**, 1319 (1999)]. The GST tag was removed by thrombin cleavage at 4°C for 2 hours, followed by purification on a Source Q column. Vesicles containing phosphatidylinositol 4-phosphate (PIP) or PIP₂ (48:48:4 of dibromo-phosphatidyl choline:phosphatidyl serine: PIP or PIP₂) were prepared by dissolving phospholipids in chloroform, drying under nitrogen, resuspending in 20 mM HEPES (pH 7.0), 100 mM NaCl, and 1 mM DTT, and passing through >10 freeze-thaw/bath sonication cycles. Approximate concentrations of PIP₂ or PIP were calculated by dividing the total concentration by two, since 50% of the total was assumed to be on the inside layer of the vesicles.
29. Cosedimentation lipid vesicle binding assays were performed as described [J. M. Kavran *et al.*, *J. Biol. Chem.* **273**, 30497 (1998)] by mixing 3 μM protein and vesicles ($\sim 20 \mu\text{M}$ PIP or PIP₂) in 20 mM HEPES (pH 7.0), 100 mM NaCl, and 1 mM DTT (total assay volume 65 μl), incubating at 25°C for 10 min, and centrifuging at 100,000g for 1 hour. The vesicle pellet was washed with 200 μl of buffer and suspended in a volume of buffer equal to the supernatant. Bound (pellet) and unbound proteins (supernatant) were identified by SDS-PAGE.
30. Supplemental figures are available at www.sciencemag.org/feature/data/1054208.shl
31. Although we found that repressed mini-N-WASP

still interacts with Arp2/3, we do not know whether Arp2/3 binds to a composite site including elements from both the VCA and B-CBD fragments (as modeled in Fig. 2D), or if it only interacts with the B-CBD site. We only know that the second binding site helps shift the VCA-Arp2/3 complex into a nonproductive conformation.

32. M. G. Rudolph *et al.*, *J. Biol. Chem.* **273**, 18067 (1998).

33. Simulation of cooperativity model. The fractional activity of N-WASP was calculated to be

$$\theta = \frac{K_A[A] + K_B[B] + c[A][B]}{K_A K_B + K_A[A] + K_B[B] + c[A][B]}$$

where $[W]$ is the concentration of mini-N-WASP, $[A]$ is the total concentration of input molecule A, $[B]$ is the total concentration of input molecule B, c is the cooperativity factor linking binding of A and B, and

$$K_A = \frac{[W][A]}{[W \cdot A]} \quad K_B = \frac{[W][B]}{[W \cdot B]}$$

$$\frac{K_A}{c} = \frac{[W \cdot B][A]}{[W \cdot A \cdot B]} \quad \frac{K_B}{c} = \frac{[W \cdot A][B]}{[W \cdot A \cdot B]}$$

This model assumes that $[W_{tot}] \ll [A]$ and $[B]$, and that species WA, WB, and WAB have equal activity (W is inactive). Theoretical curves describing the behavior for different values of c were calculated

using the program Mathematica (Wolfram Research, www.wolfram.com).

34. R. Rohatgi, H. H. Ho, M. W. Kirschner, *J. Cell Biol.* **150**, 1299 (2000).

35. We thank J. Zalevsky for reagents and helpful discussions and H. Bourne, V. Denic, D. Julius, B. Kelch, H. Madhani, J. Weissman, and members of the Lim lab for comments and discussion. Supported by grants to W.A.L. from NIH, the Burroughs Wellcome Young Investigator Program, the Searle Scholars Program, and the Packard Foundation. K.E.P. is a Cancer Research Institute Postdoctoral Fellow.

20 July 2000; accepted 18 September 2000

Direct Coupling Between Meiotic DNA Replication and Recombination Initiation

Valérie Borde,¹ Alastair S. H. Goldman,² Michael Lichten^{1*}

During meiosis in *Saccharomyces cerevisiae*, DNA replication occurs 1.5 to 2 hours before recombination initiates by DNA double-strand break formation. We show that replication and recombination initiation are directly linked. Blocking meiotic replication prevented double-strand break formation in a replication-checkpoint-independent manner, and delaying replication of a chromosome segment specifically delayed break formation in that segment. Consequently, the time between replication and break formation was held constant in all regions. We suggest that double-strand break formation occurs as part of a process initiated by DNA replication, which thus determines when meiotic recombination initiates on a regional rather than a cell-wide basis.

During meiosis in most organisms, division of the diploid genome among haploid gametes is accompanied by frequent recombination between homologous parental chromosomes. Recombination occurs after meiotic DNA replication but before the first meiotic division. In the yeast *Saccharomyces cerevisiae*, blocking meiotic replication has been shown to prevent recombination (1–4), but the connection between these two fundamental processes remains unknown. A replication dependence of meiotic recombination would be expected if replication-inhibited cells could not form the double-strand breaks (DSBs) that initiate recombination. This could result either from a direct coupling between replication and DSBs or from checkpoint systems that sense incomplete replication and prevent DSB formation.

To test these suggestions, we examined DSBs in cells undergoing meiosis in the presence of 100 mM hydroxyurea (HU), a concentration that prevents DNA replication (4). In such conditions, meiotic progression is

normally blocked before the first nuclear division (meiosis I) by the *MEC1*-dependent checkpoint system; progression is restored in *mec1-1* mutants (4). Wild-type cells sporulated in HU did not form DSBs, and meiotic progression was blocked (5). By contrast, about 40% of *mec1-1* mutant cells progressed through the meiosis I in the presence of HU, but DSBs still did not form (Fig. 1). Thus, the failure to form DSBs without replication is not due to a *MEC1*-dependent checkpoint block to meiotic progression, making it likely that replication is directly required for DSB formation. This conclusion is reinforced by the finding that *clb5 clb6* double mutants, which prevent meiotic replication without inducing the *MEC1* block (4), also fail to form DSBs (6).

To further examine the relation between replication and DSBs, we used two methods to delay replication in the left arm of chromosome III (*chrIII-L*). One approach used an *ars305 ars306 ars307* triple mutation to inactivate all meiotic replication origins on *chrIII-L* (7) (Fig. 2A). The *ars305 ars306 ars307 chrIII-L* is replicated passively by forks initiating at *ARS309* on the right arm (*chrIII-R*) or further to the right, at least 126 kb from the left-hand telomere. On the basis of a fork progression rate of 2 kb/min (8), replication of the *ars305 ars306 ars307 chrIII-L* should take at least 40 min longer

than when these origins are present and active. The other approach used a reciprocal translocation (*his4::TEL1-L*, Fig. 2A), replacing the first 70 kb of chromosome III with the first 4 kb of chromosome I (*TEL1-L*). This places *TEL1-L* next to the *HIS4-CEN3* region, which undergoes frequent DSBs (9) and contains the early-firing origin *ARS306* (10). Yeast telomeres are late replicating and impose this property on nearby sequences (11, 12), so this translocation should delay replication in the *HIS4-CEN3* region.

We monitored meiotic replication on chromosome III by two-dimensional (2D) gel electrophoresis of replication intermediates (13). Replication occurred simultaneously at three locations on the normal chromosome III (Fig. 2D). By contrast, in *ars305 ars306 ars307* strains, replication on *chrIII-L* was delayed by 60 min relative to *chrIII-R* (Fig. 2, B and D), as expected if *chrIII-L* was replicated passively by forks initiating on *chrIII-R*. On *his4::TEL1-L*, replication in the *HIS4-CEN3* region was delayed by 30 min relative to *chrIII-R* (Fig. 2D), and most *ARS306* origin activity was eliminated (5), as expected for a telomere position effect on replication.

Delaying replication did not markedly affect DSB frequencies on *chrIII-L*, as measured from blots of pulsed-field gels (Fig. 2C). Maximum DSB levels on the *ars305 ars306 ars307 chrIII-L* were identical to those on the normal chromosome ($20\% \pm 6\%$ compared with $20\% \pm 5\%$), as were break levels at individual sites (5). DSBs between *HIS4* and *CEN3* on *his4::TEL1-L* were modestly reduced ($6 \pm 2\%$ compared with $12 \pm 2\%$ on a normal chromosome), the reduction being stronger near *TEL1* than near *CEN3*. However, delaying replication locally had a distinct, reproducible effect on DSB timing (Fig. 2, C and D). DSBs formed simultaneously (1.5 to 2 hours after replication) in both arms of the normal chromosome III. By contrast, overall DSB formation in the late-replicating *ars305 ars306 ars307 chrIII-L* was delayed by 30 min compared with *chrIII-R* (Fig. 2, C and D). Thus, the time interval between replication and DSB formation was maintained in both arms. Furthermore, the DSB delay in the originless *chrIII-L* varied with distance from active right-arm

¹Laboratory of Biochemistry, Division of Basic Science, National Cancer Institute, Bethesda, MD 20892–4255, USA. ²Department of Molecular Biology and Biotechnology, University of Sheffield, Sheffield S10 2TN, UK.

*To whom correspondence should be addressed. E-mail: lichten@helix.nih.gov

Structural Analysis of Autoinhibition in the Ras Activator Son of Sevenless

Holger Sondermann,^{1,2,5} Stephen M. Soisson,^{3,5,6}

Sean Boykevich,⁴ Shao-Song Yang,⁴

Dafna Bar-Sagi,⁴ and John Kuriyan^{1,2,*}

¹Howard Hughes Medical Institute
Department of Molecular and Cell Biology and
Department of Chemistry

University of California, Berkeley and

²Physical Biosciences Division

Lawrence Berkeley National Laboratory
Berkeley, California 94720

³Laboratories of Molecular Biophysics

The Rockefeller University

1230 York Avenue

New York, New York 10021

⁴Department of Molecular Genetics
and Microbiology

The State University of New York at Stony Brook
Stony Brook, New York 11794

Summary

The classical model for the activation of the nucleotide exchange factor Son of sevenless (SOS) involves its recruitment to the membrane, where it engages Ras. The recent discovery that Ras•GTP is an allosteric activator of SOS indicated that the regulation of SOS is more complex than originally envisaged. We now present crystallographic and biochemical analyses of a construct of SOS that contains the Dbl homology-pleckstrin homology (DH-PH) and catalytic domains and show that the DH-PH unit blocks the allosteric binding site for Ras and suppresses the activity of SOS. SOS is dependent on Ras binding to the allosteric site for both a lower level of activity, which is a result of Ras•GDP binding, and maximal activity, which requires Ras•GTP. The action of the DH-PH unit gates a reciprocal interaction between Ras and SOS, in which Ras converts SOS from low to high activity forms as Ras•GDP is converted to Ras•GTP by SOS.

Introduction

The signaling protein Ras is a molecular switch that cycles between inactive GDP bound and active GTP bound states (Vetter and Wittinghofer, 2001). Receptors that signal through tyrosine kinases activate Ras by recruiting the Ras-specific nucleotide exchange factor Son of sevenless (SOS) to the plasma membrane, where SOS and Ras form a complex that results in the expulsion of otherwise tightly bound nucleotides from Ras (Yarden and Sliwkowski, 2001; Nimnual and Bar-Sagi, 2002; Boriack-Sjodin et al., 1998). Ras is kept under strict control in the cell, and the unregulated activation

of Ras is a consistent hallmark of many cancers (Coleman et al., 2004).

SOS is a complex multidomain protein of about 1330 residues (Figure 1A). The N-terminal domain (~200 residues) contains two tandem histone folds of unknown function (Sondermann et al., 2003) and is followed by a Dbl homology (DH) domain (~200 residues) and a pleckstrin homology (PH) domain (~150 residues) that together are implicated in the activation of the small GTPase Rac1 (Nimnual et al., 1998; Soisson et al., 1998). The next two domains are both required for the Ras-specific nucleotide exchange activity of SOS and are always found together in other Ras-specific nucleotide exchange factors. The first of these is the Ras exchanger motif (Rem) domain (~200 residues), which is followed by the Cdc25 domain (~300 residues; named for homology to Cdc25, the Ras activator protein in yeast) (Boriack-Sjodin et al., 1998). We refer to these two domains together as SOS^{cat}. Finally, the ~250 residues in the C-terminal region provide docking sites for adaptor proteins such as Grb2 (Buday and Downward, 1993; Egan et al., 1993; Gale et al., 1993; Li et al., 1993).

The structure of nucleotide-free Ras in complex with SOS^{cat} showed that Ras is bound in such a way that its nucleotide binding site is almost completely disrupted (Boriack-Sjodin et al., 1998). The interaction between Ras and SOS is localized entirely to the Cdc25 domain, and the position and function of the Rem domain, which interacts with a surface of the Cdc25 domain that is distal to the active site, was puzzling at first. A recent crystallographic study uncovered a role for the Rem domain in a previously unsuspected allosteric mechanism in SOS (Margarit et al., 2003). Ras•GTP, the product of the exchange reaction, interacts with a distal binding site on SOS^{cat} that is between the Rem and Cdc25 domains, thereby forming a bridge between these two domains (Figure 1A). Binding of Ras•GTP to this distal allosteric site results in increased Ras exchange activity, indicating the presence of a positive feedback loop in the activation of Ras by SOS.

Initial models for the regulation of SOS emphasized its recruitment to the membrane as the key step of activation, since Ras is membrane bound. The regulation of SOS is likely to be more complex than simple membrane recruitment. In addition to the Grb2-mediated recruitment of SOS to the plasma membrane, early experiments suggested a role for the N-terminal segment of SOS in its activation (Byrne et al., 1996). Deletion of the C-terminal docking segment or the N-terminal 550 amino acids (including the histone domain and the DH-PH unit) increases SOS activity in cellular assays (Corbally-Garcia et al., 1998; Kim et al., 1998; Qian et al., 1998). These results, as well as a recent genetic study of *Drosophila* SOS (Silver et al., 2004), suggest that there is a complex but poorly characterized interplay between the domains of SOS that results in modulation of the ability of SOS to activate Ras (Hall et al., 2002).

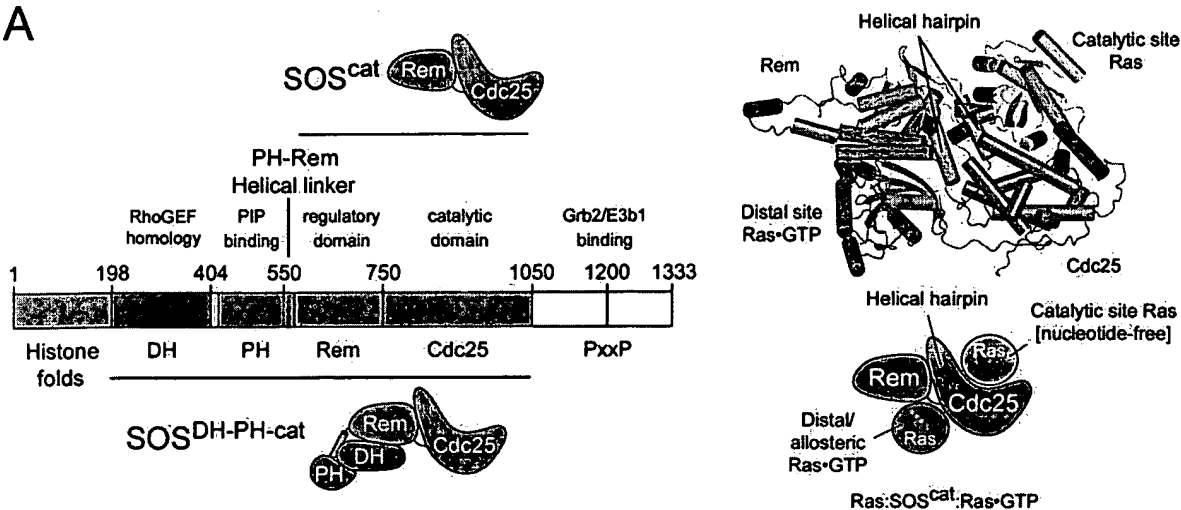
In the present study, we investigate a construct of SOS (SOS^{DH-PH-cat}) that contains the DH-PH unit in addition to the catalytic unit (SOS^{cat}). By determining the structure

*Correspondence: kuriyan@berkeley.edu

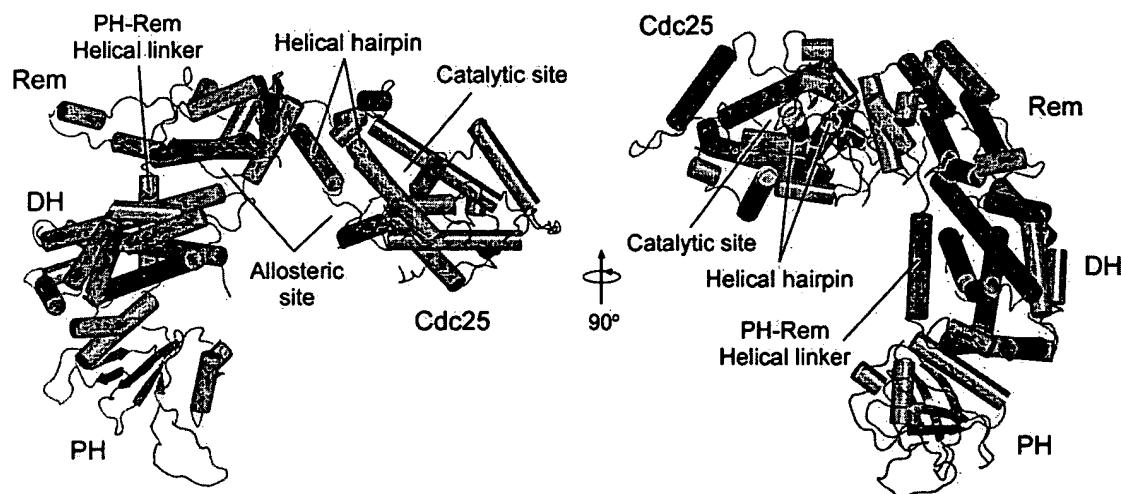
⁵These authors contributed equally to this work.

⁶Present address: Merck Research Laboratories, P.O. Box 2000, RY50-105, Rahway, New Jersey 07065.

A



B



C

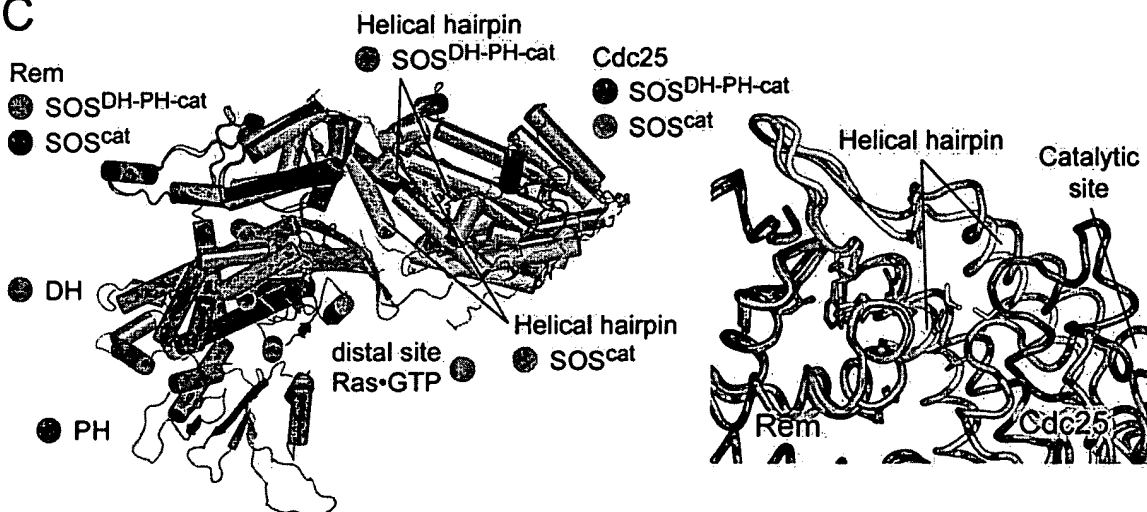


Figure 1. Structure of SOS^{DH-PH-cat}

(A) Domain organization of SOS and overview of a ternary Ras:SOS complex. The crystal structure of the Ras:SOS^{cat}:Ras^{Y64A}•GppNp ternary complex is shown (Margarit et al., 2003; PDB code 1NVV). The helical hairpin of the Cdc25 domain is shown in orange.

(B) The crystal structure of SOS^{DH-PH-cat}. Two orthogonal views are shown with coloring according to the diagram shown in (A).

(C) Comparison of SOS^{DH-PH-cat} with the structure of the ternary Ras:SOS^{cat}:Ras•GTP complex (PDB code 1NVV). The structures were aligned through superpositioning of the two respective Rem domains of SOS^{DH-PH-cat} and SOS^{cat}. Ras at the catalytic site is not shown for clarity (see [A]). Note that the distal Ras^{Y64A}•GppNp (green) in the ternary complex overlaps with the DH domain of SOS^{DH-PH-cat}. A close-up view of the Rem-Cdc25 interface is shown (right).

of SOS^{DH-PH-cat}, we show that the DH-PH unit inhibits SOS by blocking the distal allosteric Ras•GTP binding site of SOS. Surprisingly, blockage of the allosteric Ras binding site suppresses both the unstimulated (by Ras•GTP) and the allosterically stimulated levels of activity of SOS, leading to the discovery that the basal level of SOS activity is dependent on the binding of Ras•GDP to the distal site. It appears that the SOS protein has evolved to have its nucleotide exchange activity be masked until as yet undiscovered signals trigger the displacement of the DH-PH unit and the opening of the allosteric site, allowing Ras itself to stimulate SOS to first low and then high levels of activity.

Results and Discussion

Crystal Structure of SOS^{DH-PH-cat}

We determined the crystal structure of SOS^{DH-PH-cat} at 3.62 Å resolution using phases determined experimentally to 4.0 Å resolution (see Experimental Procedures and Supplemental Tables S1 and S2 at <http://www.cell.com/cgi/content/full/119/3/393/DC1/>). Extensive screening of crystallization conditions did not improve crystalline order, and, given the resolution of the X-ray data, we have chosen not to refine individual atomic positions. Instead, we limited model optimization to rigid-body refinement of the positions and orientations of the individual domains, which are placed with high confidence because of the excellent quality of the experimental electron density maps (see Supplemental Figure S1). These maps suggest that the structure of each domain is essentially the same as that seen previously in crystal structures of the isolated DH-PH module and the SOS^{cat} domain bound to Ras (Soisson et al., 1998; Boriack-Sjodin et al., 1998; Margarit et al., 2003).

The crystals contain two molecules of SOS^{DH-PH-cat} in the asymmetric unit, with similar structure. SOS^{DH-PH-cat} forms a curved C-shaped assembly that has the PH domain at one end and the Cdc25 domain at the other (Figure 1B). The PH domain interacts only with the DH domain, which in turn packs against the face of the Rem domain that is distal to the Cdc25 domain and makes no contact with the latter. A helical linker (residues 550–566) that is not present in previous models is seen to connect the PH and Rem domains and was traced unambiguously (Figure 1 and see Supplemental Figure S1 on the Cell web site). This linker packs against a hydrophobic patch on the DH domain, with ~1500 Å² of surface area buried at the interface, and may therefore be important in positioning the DH-PH module with respect to SOS^{cat} (Figure 1B). The internal structure of the DH-PH unit within this assembly is essentially the same as that seen previously in the structure of the isolated DH-PH domains (Soisson et al., 1998).

The general structure of the SOS^{cat} module in SOS^{DH-PH-cat} is distorted slightly with respect to that seen previously in binary or ternary complexes of SOS bound to Ras (Boriack-Sjodin et al., 1998; Margarit et al., 2003) (Figure 1C). In the two molecules in the asymmetric unit of the crystal, the Rem and Cdc25 domains are splayed apart by 20° and 28°, respectively, so that the tight contact between the Rem domain and the helical hairpin structure of the Cdc25 domain, seen in crystal structures

of SOS^{cat} bound to Ras, is broken in SOS^{DH-PH-cat} (Figure 1C). The interface between the Rem domain and the helical hairpin of the Cdc25 domain is known to be important for SOS activity (Hall et al., 2001), and the disruption of this interface correlates with the reduced level of nucleotide exchange activity exhibited by SOS^{DH-PH-cat} (see below).

A notable feature of the SOS^{DH-PH-cat} structure is the location of the DH domain, which is positioned so that it blocks the allosteric binding site for Ras (Figure 1C). This feature predicts that the nucleotide exchange activity of SOS^{DH-PH-cat} would not be readily stimulated by Ras•GTP, since the binding of Ras•GTP to the distal site would require that the DH domain swing out of the way.

The DH domain packs against the Rem domain, with an interface that is conserved in sequence from humans (SOS1 and SOS2) to *C. elegans*, and is composed mainly of polar residues (Figure 2A). There are differences in the relative positioning of the DH and Rem domains in the two molecules in the asymmetric unit, in which the DH domains are rotated by 11° with respect to one another (data not shown). Despite the loose nature of its linkage to the Rem domain, the DH domain appears to act as an efficient latch on the distal Ras binding site of SOS because of its stable positioning by the helical PH-Rem linker (Figures 1B and 1C).

The DH-PH Unit Inhibits the Ras-Specific Nucleotide Exchange Activity of SOS

In assaying the nucleotide exchange activity of SOS^{DH-PH-cat}, we take advantage of a mutant form of Ras, Ras^{Y64A}, which binds to the distal site of SOS but not to the catalytic site (Margarit et al., 2003; Hall et al., 2001; Boriack-Sjodin et al., 1998). We also discuss two mutant forms of SOS. SOS^{cat-W729E} does not bind Ras at the distal site (Figure 2B) (see below), and SOS^{DH-PH-cat-triple.mut} (E268A/M269A/D271A) has a weakened Rem-DH interface (Figure 2A). These two mutant forms of SOS are part of a large set of mutations that we have screened for activity, and, since our results are internally consistent, we focus mainly on these two for clarity. In experiments that call for Ras•GTP, we use the nonhydrolysable GTP analog GppNp instead of GTP, so that the hydrolysis of GTP by Ras is not a complicating factor. For simplicity, we refer to Ras•GppNp as “Ras•GTP.”

The autoinhibition of SOS^{DH-PH-cat} is demonstrated by an assay in which the release of fluorescently labeled GDP from Ras is monitored (Ahmadian et al., 2002) (Figure 2C). When the SOS:Ras•GDP ratio is 1:1, the release of GDP from Ras is about three times slower with SOS^{DH-PH-cat} when compared to SOS^{cat} (Figures 2C and 2F). More strikingly, SOS^{DH-PH-cat} is inert to allosteric stimulation by Ras•GTP. Whereas addition of stoichiometric amounts of Ras^{Y64A}•GTP accelerates the turnover by SOS^{cat} significantly, there is no significant increase in the rate of the SOS^{DH-PH-cat}-catalyzed nucleotide release under identical conditions (Figure 2). The addition of a 20-fold molar excess of Ras^{Y64A}•GTP to SOS^{DH-PH-cat} increases the rate of GDP release from Ras only marginally, to a level comparable of that obtained with the SOS^{cat} domain in the absence of Ras^{Y64A}•GTP (Figure 2C).

The inability of Ras•GTP to stimulate the activity of

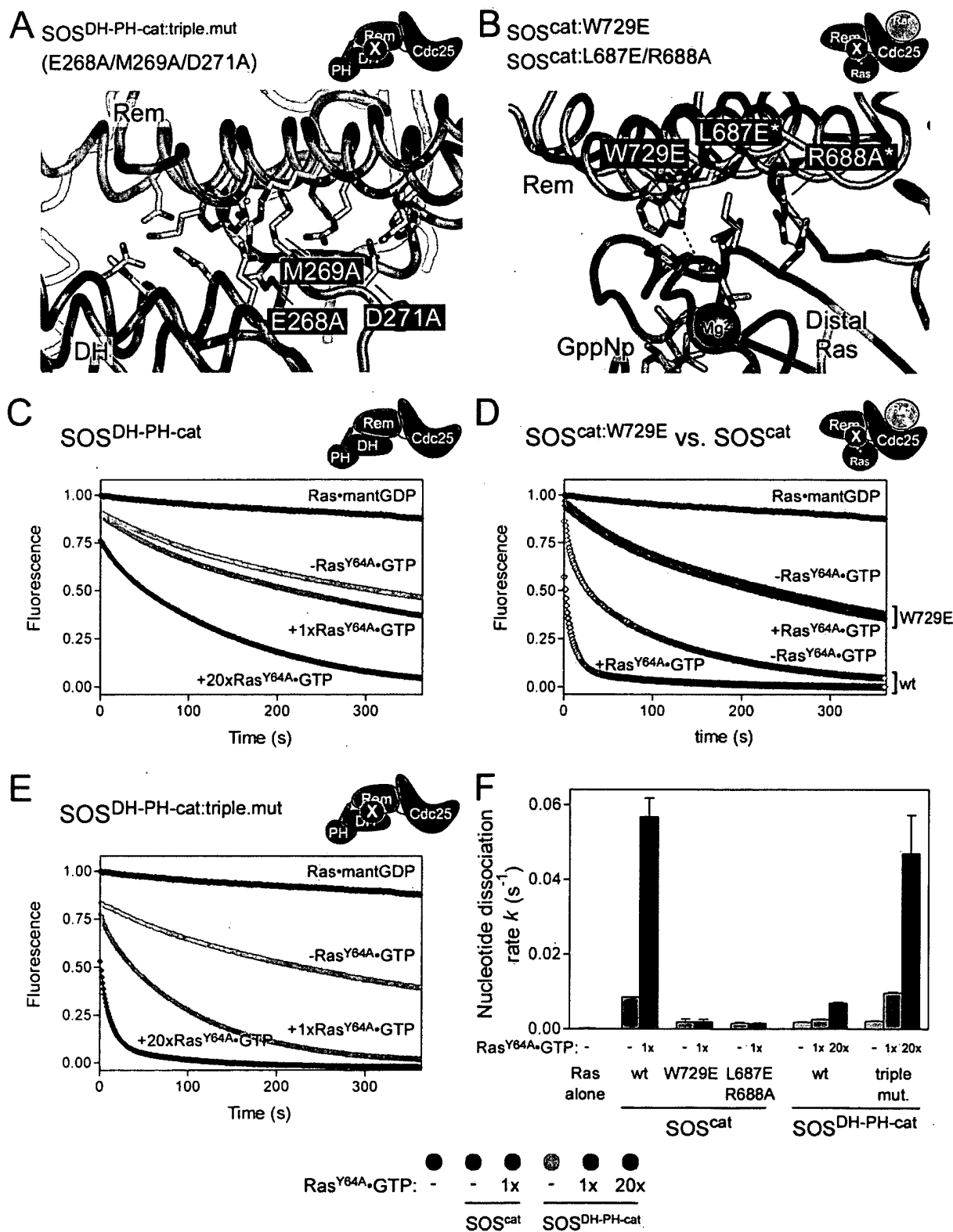


Figure 2. Kinetic Analysis of SOS^{DH-PH-cat} and Mutant Forms of SOS^{cat} and SOS^{DH-PH-cat}

(A) Interactions between the DH and Rem domains in SOS^{DH-PH-cat}. The combination of mutations analyzed in (E) and (F) and in Figure 5 are shown. (B) Interactions between the Rem domain of SOS and Ras at the distal binding site on SOS. The structure of a ternary Ras:SOS^{cat}:Ras-GTP complex is shown (PDB code 1NVV; Margarit et al., 2003). Mutations analyzed in (D) and (F) and Figures 3 and 5 are shown. Asterisks indicate double mutants.

(C) Nucleotide exchange rates for SOS^{DH-PH-cat}. Ras-mantGDP (1 μ M) was incubated in buffer containing unlabeled GDP (200 μ M) in the absence

SOS^{DH-PH-cat} is consistent with the crystal structure, in which the DH domain blocks the allosteric binding site for Ras. This naturally raises the question as to the nature of the trigger that releases this inhibition. This issue is unresolved at present, but mutations at the DH-Rem interface that are expected to destabilize the interaction between the DH and Rem domains (Figure 2A; SOS^{DH-PH-cat(triple.mut)}) have the effect of partially relieving the inhibitory effect of the DH domain on the stimulation of SOS^{DH-PH-cat} by Ras•GTP (Figures 2E and 2F; a cell-based assay of this mutant is discussed in a later section). Although the basal activity of SOS^{DH-PH-cat(triple.mut)} is not increased significantly compared to wild-type (Figures 2C and 2E), the mutant protein is more readily stimulated by the addition of Ras•GTP. Addition of Ras^{Y64A}•GTP, in a stoichiometry of 1:1 relative to SOS^{DH-PH-cat(triple.mut)}, yields nucleotide exchange rates that are comparable to those of the isolated, unstimulated SOS^{cat} domain, and a 20-fold molar excess of Ras^{Y64A}•GTP increases the rate to the maximal level observed when SOS^{cat} is stimulated by Ras•GTP (Figures 2E and 2F).

Blockage of the Distal Ras Binding Site Decreases the Affinity of SOS for Ras at the Catalytic Site

To further assess the autoinhibition of SOS experimentally, we measured the affinity of Ras for the catalytic site of SOS by using fluorescence anisotropy. In these experiments, we use Oregon green-labeled Ras (see Experimental Procedures) that can, in principle, bind to either the active site of SOS or the distal site. The experiments are set up so that the distal site is either blocked, as in SOS^{DH-PH-cat} or SOS^{cat}:Ras^{Y64A}•GTP, or disrupted by mutation, as in SOS^{cat}:W729E (see below) (Figures 3 and 5). Our analysis is thus interpreted in terms of the binding of Ras at the catalytic site.

It is intriguing that the presence of the DH-PH unit in SOS^{DH-PH-cat} not only blocks the binding of the allosteric Ras•GTP, as is expected from the crystal structure, but also reduces the affinity of the catalytic site for Ras (Figure 3). Similar results are obtained for SOS^{cat}:W729E, which does not bind Ras at the distal site. From the titration curves, we estimate that Ras has relatively low affinity for the catalytic sites of SOS^{DH-PH-cat} and the SOS mutant that cannot bind the distal Ras (SOS^{cat}:W729E) ($K_d \sim 29.9 \mu\text{M}$ and $\sim 14.5 \mu\text{M}$, respectively) (Figure 3). In contrast, when we load the distal site of SOS^{cat} with Ras^{Y64A}•GTP, added in 10-fold molar excess to saturate the distal site, the affinity for Ras at the catalytic site is significantly higher ($K_d \sim 1.9 \mu\text{M}$). The ability of Ras bound to the distal site to increase the affinity of Ras

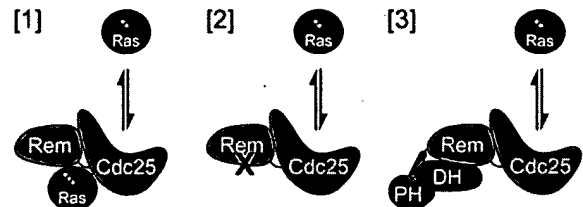
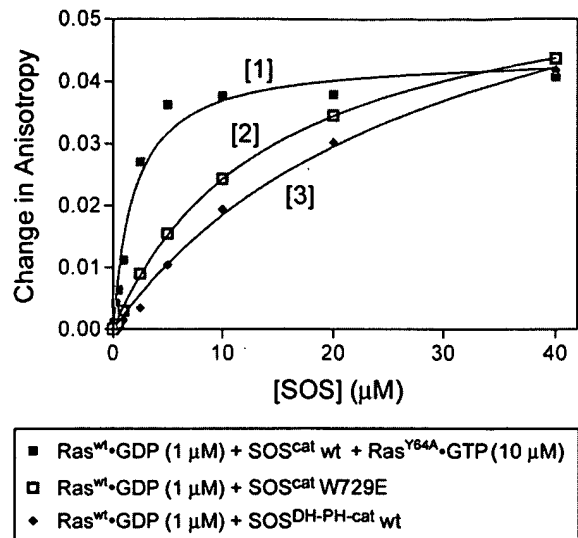


Figure 3. Binding of Ras to the Catalytic Site of SOS

Ras^{C118S/A122C} was labeled with Oregon green and loaded with GDP. Fluorescence anisotropy was used to measure the affinity of Ras^{C118S/A122C}•GDP (1 μM) for the catalytic site of SOS^{cat}:W729E, SOS^{cat}:Ras^{Y64A}•GppNp (10 μM), and SOS^{DH-PH-cat}. The fluorescence anisotropy of Ras^{C118S/A122C}•GDP alone was subtracted from each data point of the titration. Affinities were estimated by nonlinear regression (K_d , Ras•GDP:SOS^{cat}:W729E $\sim 14.5 \mu\text{M}$; K_d , Ras•GDP:SOS^{cat}:Ras^{Y64A}•GppNp $\sim 1.9 \mu\text{M}$; K_d , Ras•GDP:SOS^{DH-PH-cat} $\sim 29.9 \mu\text{M}$).

for the catalytic site of SOS is likely to be a key component of the mechanism by which Ras stimulates the activity of SOS.

Crystal Structure of a Ras:SOS^{cat}:Ras^{Y64A}•GDP Complex

The structure of SOS^{DH-PH-cat} explains the inability of Ras•GTP to stimulate nucleotide exchange activity robustly, since the distal binding site is blocked. The structure does not provide a ready explanation for our observation that the basal level of activity displayed by SOS^{DH-PH-cat} (i.e., unstimulated by Ras•GTP) is lower than

or presence of SOS^{DH-PH-cat} (1 μM). The release of labeled nucleotide in the presence of stoichiometric amounts of Ras^{Y64A}•GppNp (1 \times and 20 \times) is shown.

(D) Comparison of SOS^{cat}- and SOS^{cat}:W729E-mediated nucleotide release. The assay conditions are identical to (C), except that the wild-type and the mutant form of SOS^{cat} (see [B]) were used.

(E) Nucleotide exchange by SOS^{DH-PH-cat} with mutations in the DH:Rem domain interface. The assay conditions are identical to (C), except that the mutant form of SOS^{DH-PH-cat}, SOS^{DH-PH-cat(triple.mut)} (see [A]), was used.

(F) Comparison of nucleotide exchange rates of wild-type and mutant forms of SOS^{DH-PH-cat} and SOS^{cat}. Rates were fitted to single exponentials. Error bars indicate standard deviations of three independent experiments. Colors are consistent with (C), (D), and (E). Orange bars represent the basal, unstimulated SOS^{DH-PH-cat}-mediated exchange rate; gray and red bars show rates in presence of 1 μM and 20 μM Ras^{Y64A}•GTP, respectively. SOS^{cat}-catalyzed exchange rates in the absence and presence of Ras^{Y64A}•GTP are shown in olive and green, respectively. Nucleotide exchange rates for wild-type SOS^{cat} and two mutant variants, SOS^{cat}:W729E and SOS^{cat}:L687E/P688A (see [B]), are shown.

that for SOS^{cat} in the absence of Ras•GTP (Figures 2C and 2F). The DH domain in SOS^{DH-PH-cat} makes no contact with the Cdc25 domain, and electron density maps reveal no evidence for significant structural changes within the Rem or Cdc25 domains of SOS^{DH-PH-cat}, thus ruling out any obvious mechanism for the transmission of conformational changes that might couple DH-Rem interactions to changes at the Cdc25 active site.

It occurred to us that the most ready explanation for the observed breakage of the Rem-Cdc25 interactions in SOS^{DH-PH-cat} is that this interface might be intrinsically unstable in the absence of Ras bound at the distal binding site (Figure 1C). We have shown previously that Ras•GTP binding to the distal site brings these two domains of SOS^{cat} closer together, thereby stabilizing the helical hairpin of the Cdc25 domain, a structural element that is critical for Ras binding at the active site (Margarit et al., 2003). In this section, we present a crystal structure of a ternary complex of Ras:SOS^{cat}:Ras^{Y64A}•GDP. This structure demonstrates that Ras•GDP can also provide the bridging function at the distal site, suggesting that the decreased nucleotide exchange levels of SOS^{DH-PH-cat} and SOS^{cat:W729E} are due to lack of Ras binding at the distal site.

Crystals of the ternary Ras:SOS^{cat}:Ras•GTP complexes that we have reported on earlier were obtained by purifying these complexes by gel filtration chromatography. Ras^{Y64A}•GDP binds to SOS^{cat} with too low an affinity for the isolation of ternary complexes by gel filtration chromatography. Instead, we obtained crystals of such a complex by adding a 4-fold molar excess of Ras^{Y64A}•GDP to a binary Ras:SOS^{cat} complex and setting up crystallization trials with these solutions. Crystals were obtained under conditions that are similar to those described previously for the Ras:SOS^{cat}:Ras•GTP complexes (see Experimental Procedures; Margarit et al., 2003). Diffraction data to 2.7 Å resolution were collected using synchrotron radiation, and structure determination was straightforward because the space group and unit cell dimensions (space group I422, $a = b = 183.7$ Å, $c = 177.8$ Å, one complex in the asymmetric unit) are similar to those of the ternary Ras•GTP complex.

The structure of the Ras:SOS^{cat}:Ras^{Y64A}•GDP complex closely resembles that of the ternary Ras:SOS^{cat}:Ras•GTP complexes determined previously, except that the nucleotide binding site of the distal (allosteric) Ras is occupied by GDP and a phosphate ion (P_i), instead of GTP (Figure 4A). Difference electron density maps reveal a break in electron density between the β -phosphate of the bound nucleotide and the phosphate ion (Figure 4A). The distance between the β -phosphate of GDP and the phosphate ion (4.1 Å) is significantly larger than that between the β - and γ -phosphates of the nucleotide in Ras•GTP and Ras•GppNp (~ 3 Å) (Figures 4A and 4B). Furthermore, refinement with GTP instead of GDP modeled at the Ras active site results in strong negative electron density across the terminal phosphate bond and strong positive density for a dissociated phosphate ion, consistent with the nucleotide bound state being GDP•P_i•Mg²⁺ (Figure 4C).

Ras•GDP•P_i bound at the distal site of SOS adopts a conformation that is characteristic of Ras•GTP, confirming that the distal site has primary specificity for

Ras•GTP (Figures 4D and 4E) (Pai et al., 1990; Milburn et al., 1990). The coordination of empty Ras at the catalytic site of SOS is identical in both ternary complexes, with either Ras•GTP or Ras•GDP•P_i bound at the distal site, demonstrating that the binding of Ras•GDP at the allosteric site accomplishes the same structural effects at the active site of SOS^{cat} as does the binding of Ras•GTP. The phosphate ion concentration in the crystallization condition is 1.2 M, which might account for the presence of free phosphate at the nucleotide binding site. Binding measurements carried out in the absence of added phosphate ion (see below) demonstrate that this is not a requirement for Ras•GDP binding to the distal site.

Significant differences between the structures of Ras•GTP and Ras•GDP•P_i bound to the distal site are localized mainly to the switch 2 region (Figure 4D), with switch 1 of Ras•GDP•P_i being essentially in the conformation seen previously for Ras•GTP complexes. Gln-61 in switch 2 is pushed outwards by the phosphate ion, and the switch region adjusts accordingly. The coordination of GDP•P_i in Ras is similar to that seen in Arl2, another GTPase whose structure has been solved with GDP•P_i•Mg²⁺ bound at the active site (Hanzal-Bayer et al., 2002). The Arl2 structure was determined in complex with an effector protein, phosphodiesterase δ , the presence of which may stabilize the GTP bound conformation of the switch regions even in the presence of GDP•P_i.

Affinity of Ras for the Distal/Allosteric Site on SOS

We determined the affinity of Ras^{Y64A} for the distal site in SOS by fluorescence anisotropy measurements using an Oregon green-labeled mutant variant of Ras^{Y64A} (see Experimental Procedures). The change in fluorescence anisotropy upon addition of SOS reflects the formation of a Ras:SOS complex in solution (Figure 5A). The affinity of SOS^{cat} for Ras^{Y64A}•GTP at the distal site is relatively high ($K_d \sim 3.6$ μ M). Ras^{Y64A}•GDP shows weaker binding ($K_d \sim 24.5$ μ M) (Figure 5A). This is consistent with nucleotide exchange assays, in which an ~ 10 -fold excess of Ras^{Y64A}•GDP over SOS^{cat} provides the same stimulation as a 1:1 ratio of Ras^{Y64A}•GTP and SOS^{cat} (Supplemental Figure S2).

As a control, the titrations were repeated with SOS^{cat:W729E}, the mutant form of SOS that is not expected to bind Ras at the distal site because of the critical role of Trp-729 in coordinating Ras residues (Figure 2B). No significant change in fluorescence anisotropy was observed during the titration for Ras^{Y64A} loaded with GDP or GTP, indicating that the change in fluorescence anisotropy observed with wild-type SOS^{cat} corresponds to Ras binding at the distal site (Figures 5A and 5B).

To compare the binding of Ras at the distal site in wild-type and mutant forms of SOS^{DH-PH-cat}, we measured the fluorescence anisotropy using a concentration of SOS and Ras such that binding of SOS^{cat} to Ras^{Y64A}•GTP is almost maximal and binding of Ras^{Y64A}•GDP is clearly detectable (see arrow in Figure 5A). Titrations for Ras^{Y64A}•GTP binding to SOS^{DH-PH-cat} and a mutant form, SOS^{DH-PH-cat:triple mut} (E268A/M269A/D271A, Figure 2A), are shown as Supplemental Data (Supplemental Figure

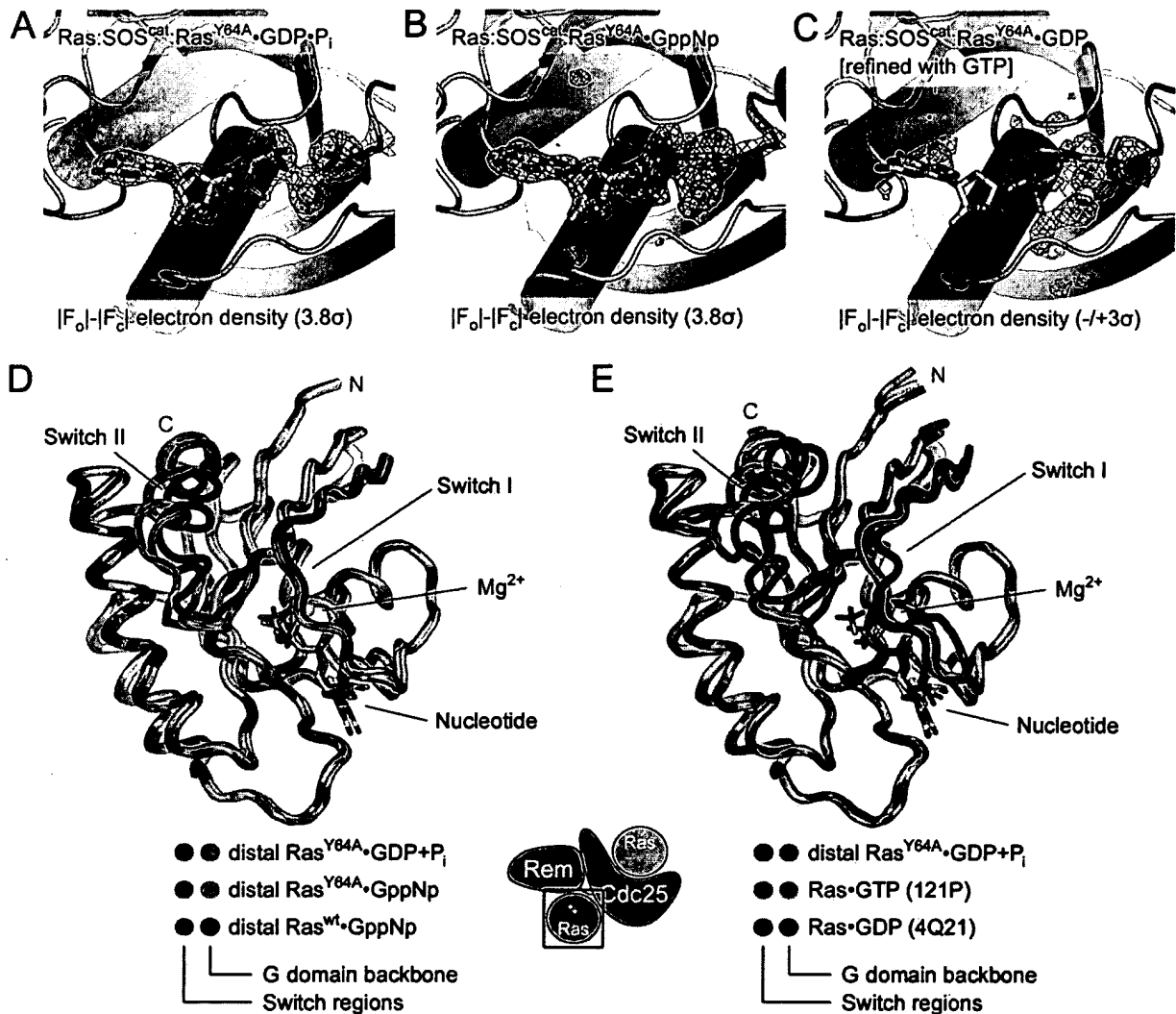


Figure 4. Structure of a Ras:SOS^{cat}:Ras^{Y64A}•GDP Complex

(A) Distal Ras^{Y64A}•GDP•P_i in the structure of the ternary complex. The electron density map shown has amplitudes of (|F_o| - |F_c|), with F_o and F_c being the observed and calculated structure factors. Phases were calculated from a model at a stage of the refinement prior to inclusion of nucleotide. The blue electron density contour is at 3.8σ. Mg²⁺ is shown as a yellow sphere.

(B) Distal Ras^{Y64A}•GppNp in the structure of the ternary Ras:SOS^{cat}:Ras^{Y64A}•GppNp complex (Margarit et al., 2003). The electron density map shown was calculated as in (A), with phases calculated from a model of the Ras:SOS^{cat}:Ras^{Y64A}•GppNp complex (PDB code 1NVV) at a stage of the refinement prior to inclusion of nucleotide. The electron density contour is at 3.8σ.

(C) Distal Ras in the ternary Ras:SOS^{cat}:Ras^{Y64A}•GDP•P_i complex, refined with GTP instead of GDP bound to Ras. In this case, the phases used to calculate the electron density map were derived from a model that included GTP, with (|F_o| - |F_c|) amplitudes. Positive density is shown in blue, and negative density is shown in red. The electron densities are contoured at 3σ and -3σ, respectively.

(D) Comparison of distal Ras conformations in Ras:SOS^{cat}:Ras•GXP complexes. Distal Ras•GppNp from structures of ternary complexes (PDB codes 1NVV [gray] and 1NVW [black]) were superimposed on Ras^{Y64A}•GDP•P_i (orange) from the ternary complex. Switch 1 and 2 regions are highlighted (blue, Ras^{Y64A}•GDP•P_i; magenta, Ras^{Y64A}•GppNp; green, Ras^{wt}•GppNp).

(E) Comparison of distal Ras in the Ras:SOS^{cat}:Ras^{Y64A}•GDP•P_i complexes with conformations of free Ras. Distal Ras^{Y64A}•GDP•P_i from the ternary complex structure was superimposed on Ras•GTP (PDB code 121P) and Ras•GDP (PDB code 4Q21). Switch 1 and 2 regions are highlighted (blue, Ras^{Y64A}•GDP•P_i; red, Ras^{wt}•GDP; green, Ras^{wt}•GTP).

S3A). SOS^{DH-PH-cat} does not bind Ras^{Y64A}•GTP to a significant level, consistent with results reported above (Figures 2C and 5B). A mutant form of SOS^{DH-PH-cat} (SOS^{DH-PH-cat:triple.mut.}, E268A/M269A/D271A, Figure 2A), in which the Rem-DH interface is weakened by replacing three interfacial residues by alanine (Figure 2A), shows detectable binding of Ras^{Y64A}•GTP (Figure 5B) and, to a lesser extent, Ras^{Y64A}•GDP (Supplemental Figure S3B).

This mutant form of SOS^{DH-PH-cat} also shows significant activation by allosteric Ras^{Y64A}•GTP (Figures 2E and 2F).

Mutations in SOS^{cat} that Block Distal Ras Binding Mimic the Autoinhibited State of SOS^{DH-PH-cat}

Taken together, our results suggest that a primary role of the DH domain in the autoinhibitory mechanism is to block the binding of Ras•GDP and Ras•GTP to the distal

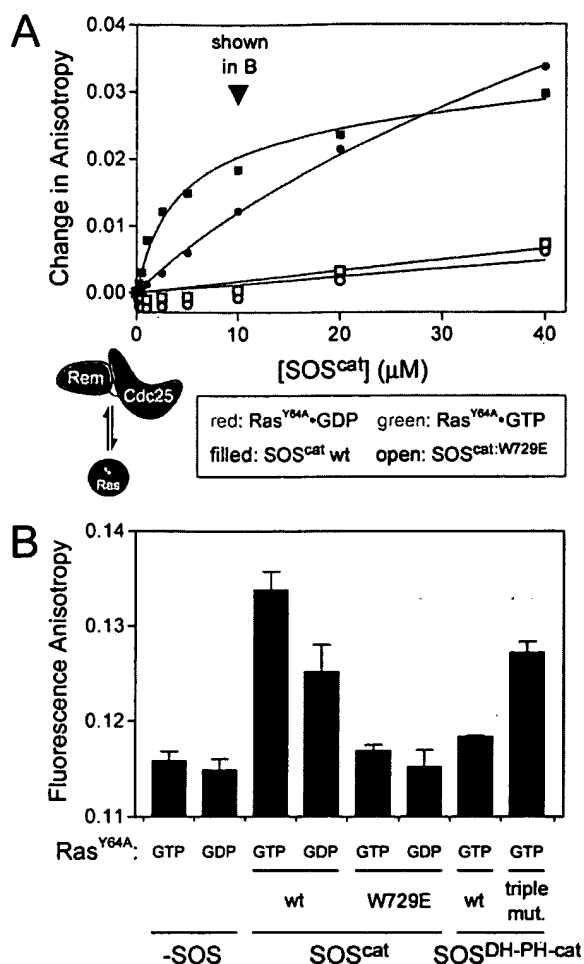


Figure 5. Binding of Ras to the Distal Site of SOS

(A) Binding of Ras^{Y64A} to the distal binding sites of SOS. Binding of Oregon green-labeled Ras^{Y64A/C118S/A122C} to SOS^{cat} was monitored by changes in fluorescence anisotropy. Ras^{Y64A/C118S/A122C} (1 μM) was loaded with GppNp (green) or GDP (red). Increasing amounts of wild-type SOS^{cat} (filled symbols) or SOS^{cat}W729E (open symbols) were added. The fluorescence anisotropy of Ras^{Y64A/C118S/A122C} alone was subtracted from each data point of the titration. Affinities were estimated by nonlinear regression (K_d , Ras^{Y64A}•GppNp:SOS^{cat} ~3.6 μM; K_d , Ras^{Y64A}•GppNp:SOS^{cat} ~24.5 μM; no binding to SOS^{cat}W729E). (B) Ras^{Y64A} binding to SOS^{cat} and SOS^{cat}-PH-cat. Fluorescence anisotropy of labeled Ras^{Y64A/C118S/A122C} (1 μM) was measured in the absence and presence of wild-type SOS^{cat}, SOS^{cat}W729E, wild-type SOS^{cat}-PH-cat, or SOS^{cat}-PH-cat:triple mut. (10 μM). For mutant forms of SOS^{cat} and SOS^{cat}-PH-cat variants, only Ras^{Y64A/C118S/A122C}•GppNp binding is shown, since GDP-loaded Ras is expected to show weaker binding based on the results described in (A).

site, rather than to directly induce structural changes in the catalytic site of SOS. This is consistent with the effects of mutations in SOS^{cat} that disrupt the binding site for distal Ras. In nucleotide exchange assays, SOS^{cat}W729E has lower basal activity than wild-type SOS^{cat}, and the allosteric stimulation by Ras•GTP is lost, as is the case for SOS^{cat}-PH-cat (Figures 2D and 2F). We also generated another mutant form of SOS^{cat}, in which Arg-688 and Leu-687 are replaced by alanine and glutamic acid, respectively (SOS^{cat}L687E/R688A). Like Trp-729, these two residues are located at the base of the Rem domain

and interact with the switch 1 region of Ras•GTP or Ras•GDP bound at the distal site (Figure 2B). As seen for SOS^{cat}W729E, SOS^{cat}L687E/R688A has lower basal exchange activity than wild-type SOS^{cat} and is not stimulated by Ras•GTP (Figure 2F). These results point to the importance of Ras•GDP in enabling an intermediate activity of SOS, a fact that was not appreciated previously because Ras•GDP was always present in the assay solutions used to measure SOS activity.

Importance of the Allosteric Binding Site for the Activation of Ras in Cellular Assays

To further validate the relevance of the allosteric mechanism of SOS, we turned to a cell-based assay for SOS activity. COS1 cells were cotransfected with expression plasmids encoding T7-tagged SOS constructs and a vector from which HA-tagged ERK2 is expressed, as described earlier (Corbalan-Garcia et al., 1998). Transfection efficiencies were adjusted to yield similar levels of expression of the various SOS constructs. ERK2 was immunoprecipitated with anti-HA antibodies, and its kinase activity was assayed using myelin basic protein (MBP) as a generic substrate.

Expression of SOS^{cat} in cells leads to robust activation of ERK2, as seen previously (Figure 6 and Corbalan-Garcia et al. [1998]). Consistent with the results described above, the two mutant SOS^{cat} proteins that block allosteric Ras binding in vitro (SOS^{cat}W729E and SOS^{cat}L687E/R688A) are significantly impaired in their ability to stimulate ERK2 kinase activity (Figure 6A). These results provide evidence for the importance of the allosteric site of SOS for the activation of Ras in a cellular context.

Previous experiments have shown that the entire N-terminal segment of SOS, including the histone folds in addition to the DH-PH unit, inhibits SOS activity in cells (Corbalan-Garcia et al., 1998). We now show that the DH domain is the critical element of this autoinhibition. Whereas expression of constructs containing the DH domain (SOS^{cat}-DH-PH-cat and SOS^{cat}-PH-cat) result in significantly reduced stimulation of ERK2 kinase activity (Figure 6B and Corbalan-Garcia et al. [1998]), constructs lacking the DH domain, either by N-terminal or internal deletion (SOS^{cat}-PH-cat or SOS^{cat}-ADH), show levels of ERK2 activation similar to SOS^{cat}. The differences between panels A and B (Figure 6) with respect to the extent of ERK2 activation by SOS^{cat} reflect differences in SOS^{cat} expression levels due to experimental variations in transfection efficiencies. Mutations at the DH-Rem interface (SOS^{cat}-PH-cat:triple mut. and another mutant form of SOS^{cat}-PH-cat with additional mutations) partially alleviate the autoinhibition in the cell-based assay, again consistent with our in vitro data (Supplemental Figure S4).

Conclusions

The activation of Ras has profound consequences for the cell, with downstream effects ranging from alterations in cellular architecture and motility to changes in the control of cell cycle and differentiation programs (Coleman et al., 2004). Given the ability of activated Ras to so potently affect cellular function, it is perhaps to be expected that the Ras activator SOS is subject to complex regulatory control. What is surprising in our

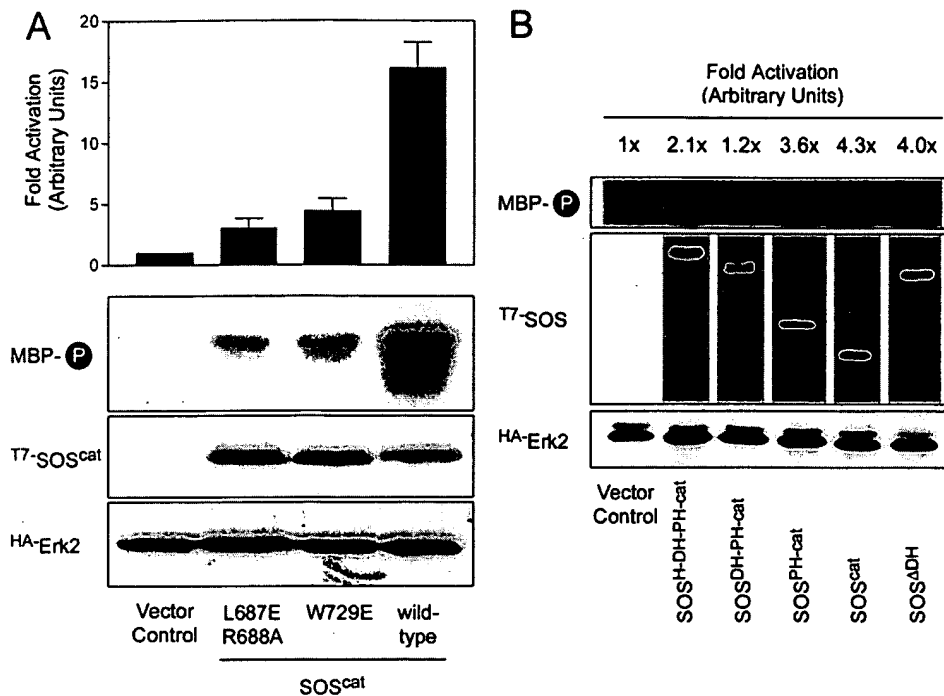


Figure 6. Activation of ERK MAP Kinase by SOS

COS1 cells were transiently cotransfected with HA-tagged ERK2 and T7-tagged SOS constructs as indicated. ERK2 activation was measured in serum-starved cells by an immunoprecipitated kinase-kinase assay using myelin basic protein (MBP) as a substrate. Results were normalized to the vector control reaction. Western blots detecting T7- and HA-tagged proteins are shown. (A) Activation of ERK2 by SOS^{cat} and SOS^{cat} mutants. Results shown in the bar diagram are from three independent experiments. Error bars indicate standard deviations of three independent experiments. The amount of ³²P incorporation into MBP was quantified by phosphorimaging. Autoradiograms and Western blots shown are from a single representative experiment. (B) Activation of ERK2 by SOS truncations. Results shown are from a single representative experiment. Experiments were repeated three times with similar results.

findings is the central role for Ras itself in determining the activation status of SOS. We had shown previously that Ras•GTP stimulates SOS to maximal levels of activity (Margarit et al., 2003). Ras•GTP binds with high affinity to the Rem and Cdc25 domains, probably stabilizing an active conformation of SOS. We have now shown that Ras•GDP binds at the same allosteric site, but with lower affinity, and sets an intermediate level of SOS activity in our assays (Figure 7A).

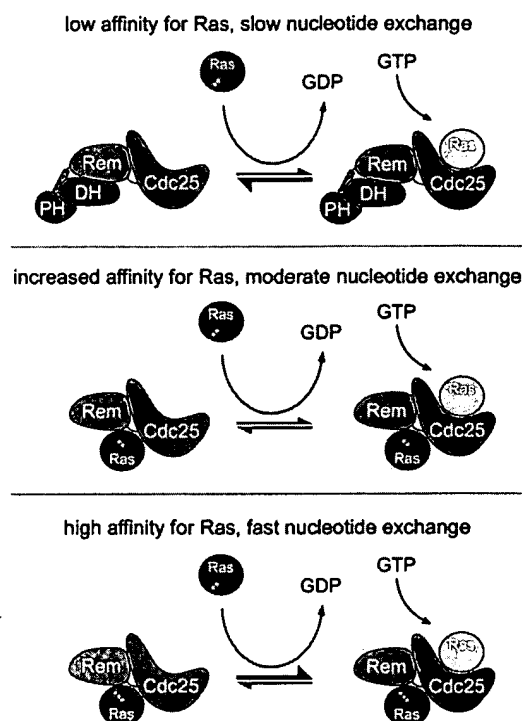
The crystal structure of SOS^{DH-PH-cat} described here reveals that the allosteric Ras binding site in SOS is blocked by the DH domain, which is located far from the active site of SOS. It appears that the DH domain has no direct inhibitory effect on the Ras-specific nucleotide exchange reaction but rather functions as a gate for Ras binding to the allosteric site.

For robust activity inside the cell, SOS would have to adopt a conformation at the membrane or in signaling complexes such that Ras has access to both the catalytic and the allosteric sites of SOS. We do not know how the inhibitory effect of the DH domain is relieved in vivo, but we expect that some sort of release mechanism will be important, since Ras•GTP binding to the distal site by itself does not seem efficient at releasing the autoinhibition mediated by the DH domain. The kinetic parameters of the reaction described here for freely diffusing proteins in solution might differ significantly when Ras:SOS complexes are tethered at the mem-

brane. Targeting of SOS to the membrane might itself be sufficient to render the enzyme active, as has been suggested earlier (Aronheim et al. 1994), perhaps through PH domain-mediated changes in conformation. Positioning of the phosphatidyl inositol binding site of SOS close to the membrane orients the remainder of SOS^{DH-PH-cat} so that both Ras binding sites of SOS are in a plane that is parallel to the membrane, indicating a conformation optimized for Ras activation and allosteric regulation (Figure 7B). Additional effectors or modifications such as phosphatidyl inositol binding by the PH domain or phosphorylation might also be involved in the activation mechanism (Sini et al., 2004; Chen et al., 1997; Das et al., 2000). The structure of the DH-PH unit, seen previously in isolation and here as part of SOS^{DH-PH-cat}, is in an inactive conformation (Soisson et al., 1998; Worthylake et al., 2000). One intriguing possibility is that events at the membrane that alter the disposition of the DH-PH unit within SOS might coordinately activate SOS for both Ras and Rac1 activation.

A recent study describes the discovery of novel mutant SOS alleles in *Drosophila* that affect SOS activity, indicating an intricate regulation of SOS in vivo (Silver et al., 2004). Mapping of these mutations to the structure presented here suggests that they might be disruptive for the DH-PH interface, the helical hairpin close to the Rem-Cdc25 interface, or the Rem domain close to the distal Ras binding site. It seems clear that further study

A Potential States of SOS Activity



B

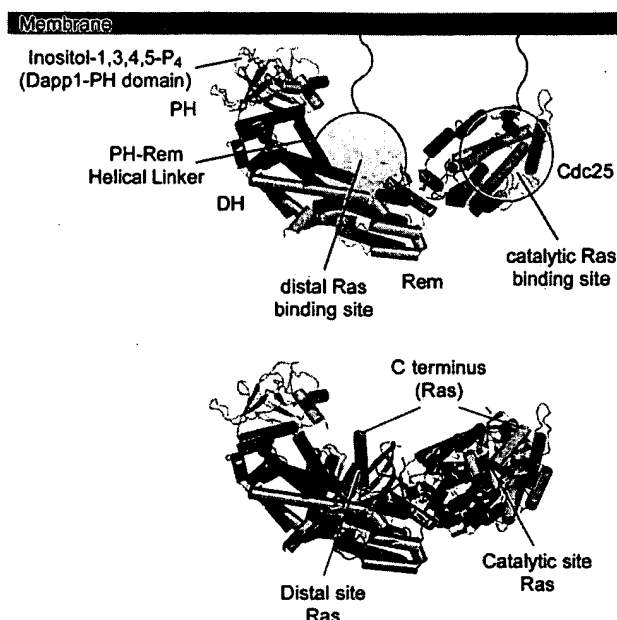


Figure 7. Models for SOS Activation

(A) Schematic diagram of potential states of SOS activity. In the autoinhibited nucleotide exchange reaction mediated by $\text{SOS}^{\text{DH-PH-cat}}$, the distal (allosteric) Ras binding site on SOS is blocked by the DH-PH unit of SOS resulting in low affinity of the catalytic site of SOS for Ras and low enzymatic activity (top). For an intermediate level of SOS activity (the SOS^{cat} -mediated nucleotide exchange), the nucleotide exchange activity of SOS is dependent on $\text{Ras}\cdot\text{GDP}$ binding to the distal binding site on SOS (middle). $\text{Ras}\cdot\text{GTP}$ binding at the distal binding site on SOS stimulates the nucleotide exchange reaction robustly (bottom).

(B) Position of the phosphatidylinositol binding site in $\text{SOS}^{\text{DH-PH-cat}}$. The Sos PH domain was superimposed with the crystal structure of the PH domain from Dapp1 (PDB code 1FA0; Ferguson et al., 2000) in complex with Inositol-1,3,4,5-tetrakisphosphate. The membrane plane is indicated. Positioning of the phosphatidylinositol binding site close to the membrane orients both Ras binding sites of SOS in a parallel plane with the membrane (bottom; see Figure 1C for details).

of the regulatory mechanism of SOS activity will be rewarding.

Experimental Procedures

Mutagenesis, Protein Expression, and Purification

$\text{SOS}^{\text{DH-PH-cat}}$ (residues 198–1049) and SOS^{cat} (residues 566–1049) of human SOS1 were cloned into the bacterial expression vector pProEx HTb (Invitrogen) using the NcoI/HindIII restriction sites. The vector fuses an N-terminal His₆ tag to the protein. *Escherichia coli* cells (BL21DE3, Novagen) were transformed with expression constructs and grown in Terrific Broth (TB) medium supplemented with 100 mg/ml Ampicillin. Protein production was induced by addition of 1 mM IPTG at a cell density corresponding to an absorbance of 1 at 600 nm, and the protein was expressed at 18°C for 16 hr. Cells were collected by centrifugation at $4000 \times g$ for 1 hr, resuspended in NiNTA buffer A (25 mM Tris-Cl [pH 7.5], 500 mM NaCl, 20 mM imidazole) containing protease inhibitors, and frozen in liquid nitrogen. Cell suspensions were thawed in a water bath at 25°C and lysed by French press (EmulsiFlex-C5, Avestin). Cell debris was removed by ultracentrifugation at $100,000 \times g$ for 1 hr at 4°C. Clear supernatants were loaded onto a NiNTA column (Qiagen) equilibrated in NiNTA buffer A. The resin was washed with 20 column volumes of the same buffer, and proteins were eluted in NiNTA buffer B (NiNTA buffer A supplemented with 500 mM imidazole). Buffers were exchanged using a Fast Desalting Column (Amersham-

Pharmacia) into TEV buffer (25 mM Tris-Cl [pH 8.3], 50 mM NaCl, 5 mM β -mercaptoethanol). His₆ tags were cleaved by incubation with Tobacco etch virus (TEV) protease, and free tags and uncleaved proteins were removed by a second NiNTA column. For $\text{SOS}^{\text{DH-PH-cat}}$ and SOS^{cat} , the flowthrough was collected and loaded onto a MonoQ column (Amersham-Pharmacia) equilibrated in MonoQ buffer A (25 mM Tris-Cl [pH 8.3], 1 mM DTT). Proteins were eluted on a gradient from 0 to 500 mM NaCl over 20 column volumes. All proteins were further subjected to size exclusion chromatography on a Superdex200 column (Amersham-Pharmacia) equilibrated in gel filtration buffer (25 mM Tris-Cl [pH 7.5], 50 mM NaCl, 1 mM DTT). Fractions containing protein were pooled and concentrated on a Centricon Ultrafiltration Device (Millipore) to a final concentration of about 50 mg/ml. Protein aliquots were frozen in liquid nitrogen and stored at -80°C .

Size exclusion chromatography coupled with static multiangle light scattering measurements was used to monitor Ras:SOS complex formation and the homogeneity of purified proteins and were performed as described previously (Margarit et al., 2003; Sondermann et al., 2003).

Point mutations were introduced into the coding region of expression plasmids using the QuikChange XL Mutagenesis Kit (Stratagene) following the manufacturer's instructions. Expression and purification of mutant proteins was identical to the procedure for wild-type proteins. All mutant proteins expressed to comparable levels. Circular dichroism spectroscopy confirmed the folded state

of the mutant SOS^{cat} proteins, with spectra undistinguishable from the wild-type protein (data not shown). Mutant Ras proteins were tested for their ability to stimulate SOS by binding to the distal site (Ras^{Y64A/C118/A122C}; Ras^{C118S/A122C}) and for their SOS-mediated nucleotide exchange reaction (Ras^{C118S/A122C}) and were found to be equally active as wild-type Ras (residues 1–166 of human Ha-Ras).

For crystallization of the ternary Ras^{wt}:SOS^{cat}:Ras^{Y64A}•GDP complex, a binary complex consisting of Ras^{wt} and SOS^{cat} was assembled as described earlier (Margarit et al., 2003). Ras^{Y64A} loaded with GDP was added in a 4-fold excess prior to crystallization.

Crystallization, X-Ray Data Collection, and Structure Solution

Initially, crystals were obtained for a fragment of human SOS1 that spans the DH-PH and Rem-Cdc25 domains (residues 189–1049; Figure 1A). Crystals of native and selenomethionine-substituted SOS^{189–1049} were obtained by hanging drop vapor diffusion. These crystals diffract X-rays to 4.0 Å (space group P2₁2₁2₁, a = 80.5 Å, b = 125.1 Å, c = 246.2 Å, with two molecules of SOS^{189–1049} in the asymmetric unit). A mercury derivative provided initial phases, which locate the positions of selenomethionines. Electron density maps calculated using experimentally determined phases to 4.3 Å, extended to 4.0 Å, were improved by B factor sharpening and by 2-fold noncrystallographic symmetry averaging.

Although at low resolution, the experimentally phased electron density maps are of high quality (Supplemental Figure S1A) and allowed each of the component domains in the two molecules to be positioned with confidence. The packing of molecules in the crystal suggested that crystallization might be improved by omitting the first nine residues of the original construct. Crystals obtained using a modified construct, SOS^{DH-PH-cat} (residues 198–1049 of human SOS1), show a slight improvement in resolution, with data measured to 3.62 Å resolution. Crystals were obtained by mixing equal volumes of protein (10–50 mg/ml) and reservoir solution (10%–14% PEG200, 10% ethylene glycol, 10 mM strontium chloride, 50 mM HEPES-NaOH [pH 6.5], and 4% sucrose). Crystals appeared within 1 hr at 20°C with typical dimensions of 0.3 mm × 0.3 mm × 0.3 mm. Crystals were frozen in propane without further cryoprotection and kept at 100 K during data collection.

Crystallographic statistics for data collection are shown in Supplemental Table S1. Data sets were collected using synchrotron radiation (ALS, Berkeley, beamline 8.2.2). Data reduction was carried out with the software package HKL2000 (Otwinowski and Minor, 1997). The space group is P2₁2₁2₁ with a = 73.5 Å, b = 127.4 Å, c = 279.1 Å. The asymmetric unit consists of two molecules of SOS^{DH-PH-cat}, and structure determination proceeded with the initial model obtained for SOS^{189–1049} for molecular replacement searches. Rigid body refinement of the individual domains of SOS using CNS (Brünger et al., 1998) yielded the final placement of the domains.

The two SOS^{DH-PH-cat} molecules in the asymmetric unit interact with their Cdc25 domains in a head-to-head fashion burying 2745 Å² of solvent-accessible surface area (data not shown). Although the binding surfaces for the noncrystallographic symmetry packing of the two protomers lie across the active site of SOS^{DH-PH-cat}, there is no indication of dimer formation of SOS^{DH-PH-cat} in solution as assayed by coupled size exclusion chromatography and multiangle light scattering measurements (data not shown).

The ternary Ras:SOS^{cat}:Ras^{Y64A}•GDP complex yielded tetragonal crystals under conditions reported previously (Margarit et al., 2003). Briefly, equal volumes of protein (20–40 mg/ml) and reservoir solution (1.2 M Na/K phosphate, 100 mM HEPES-NaOH [pH 7.5]) were mixed and incubated in hanging drops. Crystals appeared within 1 week at 4°C with dimensions of 0.03 mm × 0.02 mm × 0.02 mm. For cryoprotection, crystals were transferred to reservoir solution supplemented with 30% glycerol for 10 min, frozen in propane, and kept at 100 K during data collection.

Crystallographic statistics for data collection and refinement are shown in Supplemental Table S1. Data sets were collected using synchrotron radiation (ALS, Berkeley, beamline 8.2.1). Data reduction was carried out as previously described. The space group was determined to be I422 with similar dimensions measured for ternary Ras:SOS^{cat} complexes reported previously (a = b = 184.1 Å, c = 177.9 Å), with one complex in the asymmetric unit. The structure

was refined using standard procedures and protocols using CNS starting from a previous model (PDB code 1NVV) (Brünger et al., 1998) and O (Kleywegt and Jones, 1996).

Nucleotide Exchange Assay

Nucleotide exchange assays using mantGDP were performed as described earlier (Ahmadian et al., 2002; Margarit et al., 2003). Briefly, purified Ras (residues 1–166 of human Ha-Ras) was incubated in a 50-fold molar excess of mantGDP, GDP, or GppNp in the presence of 4 mM EDTA in gel filtration buffer. Reactions were stopped with 10 mM MgCl₂, and free nucleotide was removed by gel filtration.

Nucleotide dissociation rates were measured by incubation of 1 μM Ras•mantGDP in reaction buffer (40 mM HEPES-KOH [pH 7.5], 10 mM MgCl₂, and 1 mM DTT) supplemented with 200 μM unlabeled GDP. When indicated, reactions were supplemented with additional proteins. The data were fitted to a single exponential decay function using the program Prism (GraphPad Software Inc.). The derived rates are qualitative because of interference by unlabeled Ras•GDP at long times and low Ras•mantGDP concentrations.

Site-Specific Labeling of Proteins with Fluorescent Probes

Fluorescent maleimide derivatives (Oregon green 488) were obtained from Molecular Probes, Inc. Protein solutions were exchanged into gel filtration buffer lacking DTT prior to labeling to remove reducing agents. Proteins (5 mg/ml) were labeled in gel filtration buffer lacking DTT for 2 hr at 25°C with a 10- to 20-fold molar excess of fluorophore. Reactions were quenched by addition of 2 mM β-mercaptoethanol, and free fluorophores were removed by gel filtration using NAP5 desalting columns. Protein concentrations were determined by standard Bradford assays. Labeling efficiency was determined by UV/VIS spectroscopy on a Cary 50 Scan spectrophotometer using the molar extinction coefficient provided by Molecular Probes, Inc. The molar ratio of fluorophore to protein typically varied between 0.6 and 0.9 moles of dye per mole of protein.

Fluorescence Anisotropy Binding Assay

For detection of binding in vitro by monitoring the change of fluorescence anisotropy upon complex formation, a mutant form of Ras was used. Cys-118 is the only cysteine residue in Ras with a surface exposed sulfhydryl group, and we mutated this residue to serine (Ras^{C118S}; Kraemer et al., 2002). Next, Ala-122, which is located within a loop region of Ras and is poorly conserved, was replaced by cysteine and labeled with the fluorescent dye Oregon green 488 maleimide.

Fluorescence anisotropy assays were performed on a Spex Jobin Yvon FluoroMax-3 fluorometer. Oregon green 488-labeled Ras^{Y64A/C118S/A122C} (1 μM) or Ras^{C118S/A122C} (1 μM) was incubated with increasing amounts of SOS proteins in gel filtration buffer, and the anisotropy was measured in a 500 μl quartz cuvette at excitation and emission wavelengths of 470 nm and 515 nm, respectively, with slit bandpasses set to 2 nm. Data points were taken in triplicate after 10 min of equilibration with an integration time of 20 s per measurement.

Affinities were determined by subtraction of Ras anisotropy (no SOS added). The data were fitted to saturation binding function $F_x = (x \times B_{max}) / (K_d + x) - (NS \times x)$ where B_{max} is maximal binding, K_d is the dissociation constant, x is the concentration of SOS, and NS is a nonspecific binding constant) using the program Prism (GraphPad Software Inc.).

Ras^{C118S/A122C} and Ras^{Y64A/C118S/A122C} behave similarly to wild-type Ras and Ras^{Y64A}, respectively, in nucleotide exchange assays (data not shown).

ERK2 Immune Complex Kinase Assay

ERK2 activation was measured as described earlier (Corbalan-Garcia et al., 1998). COS1 cells, cultured in Dulbecco's modified Eagle's medium (DMEM) supplemented with 5% fetal calf serum, were transiently cotransfected with expression plasmids encoding T7-tagged SOS constructs and HA-tagged ERK2. After incubation for 24 hr in serum-free DMEM, cells were lysed in immunoprecipitation buffer (10 mM Tris-Cl [pH 7.4], 150 mM NaCl, 1% Triton X-100, 10% glycerol).

erol, 1 mM EDTA, supplemented with protease inhibitors). Protein (50 µg total) from each lysate was analyzed by SDS-PAGE and Western blotting onto nitrocellulose. Immunoblot analysis of the epitope-tagged transiently expressed proteins was carried out with anti-HA and anti-T7 antibodies followed by enhanced chemiluminescence detection. ERK2 was immunoprecipitated from lysates by using anti-HA antibody. The immune complexes were washed three times with immunoprecipitation buffer and twice with kinase buffer (25 mM Tris-Cl [pH 7.4], 20 mM MgCl₂, 2 mM MnCl₂, 1 mM Na₃VO₄, and 20 µM ATP). ERK2 kinase activity was assayed in 50 µl of kinase buffer containing 10 µCi [³²P]ATP and 0.2 mg/ml myelin basic protein (MBP). Reaction products were analyzed by SDS-PAGE and quantified with a PhosphorImager.

Acknowledgments

We are grateful to Corie Ralston, Gerry McDermott, and the scientists at beamlines 8.2.1 and 8.2.2, Advanced Light Source (ALS), Berkeley, for assistance with synchrotron data collection. Beamlines 8.2.1 and 8.2.2 at the ALS are supported by the Howard Hughes Medical Institute, and the ALS is supported by the U.S. Department of Energy's Office of Basic Energy Sciences. We are also grateful for support of the beamlines at SSRL (Stanford) and Brookhaven National Laboratories. We thank Tanya Weitz, Greg Bowman, Eric Goedken, Michelle Pirruccello, Michael Hahn, James Keller, and the Bar-Sagi Lab for valuable discussions and assistance. H.S. is supported by the Leukemia & Lymphoma Society. S.M.S. was supported by the Damon Runyon-Walter Winchell Cancer Research Foundation. D.B.-S. is supported by the NIH (grant numbers 5R37 CA55360 and 5P01 CA28146) and J.K. by the NCI (grant number R01 CA096504-02).

Received: May 20, 2004

Revised: August 30, 2004

Accepted: September 2, 2004

Published: October 28, 2004

References

- Ahmadian, M.R., Wittinghofer, A., and Herrmann, C. (2002). Fluorescence methods in the study of small GTP-binding proteins. *Methods Mol. Biol.* 189, 45–63.
- Aronheim, A., Engelberg, D., Li, N., al-Alawi, N., Schlessinger, J., and Karin, M. (1994). Membrane targeting of the nucleotide exchange factor Sos is sufficient for activating the Ras signaling pathway. *Cell* 78, 949–961.
- Boriack-Sjodin, P.A., Margarit, S.M., Bar-Sagi, D., and Kuriyan, J. (1998). The structural basis of the activation of Ras by Sos. *Nature* 394, 337–343.
- Brünger, A.T., Adams, P.D., Clore, G.M., DeLano, W.L., Gros, P., Grosse-Kunstleve, R.W., Jiang, J.S., Kuszewski, J., Nilges, M., Pannu, N.S., et al. (1998). Crystallography & NMR system: a new software suite for macromolecular structure determination. *Acta Crystallogr. D Biol. Crystallogr.* 54, 905–921.
- Buday, L., and Downward, J. (1993). Epidermal growth factor regulates p21ras through the formation of a complex of receptor, Grb2 adapter protein, and Sos nucleotide exchange factor. *Cell* 73, 611–620.
- Byrne, J.L., Paterson, H.F., and Marshall, C.J. (1996). p21Ras activation by the guanine nucleotide exchange factor Sos, requires the Sos/Grb2 interaction and a second ligand-dependent signal involving the Sos N-terminus. *Oncogene* 13, 2055–2065.
- Chen, R.H., Corbalan-Garcia, S., and Bar-Sagi, D. (1997). The role of the PH domain in the signal-dependent membrane targeting of Sos. *EMBO J.* 16, 1351–1359.
- Coleman, M.L., Marshall, C.J., and Olson, M.F. (2004). RAS and RHO GTPases in G1-phase cell-cycle regulation. *Nat. Rev. Mol. Cell Biol.* 5, 355–366.
- Corbalan-Garcia, S., Margarit, S.M., Galron, D., Yang, S.S., and Bar-Sagi, D. (1998). Regulation of Sos activity by intramolecular interactions. *Mol. Cell. Biol.* 18, 880–886.
- Das, B., Shu, X., Day, G.J., Han, J., Krishna, U.M., Falck, J.R., and Broek, D. (2000). Control of intramolecular interactions between the pleckstrin homology and Dbl homology domains of Vav and Sos1 regulates Rac binding. *J. Biol. Chem.* 275, 15074–15081.
- Egan, S.E., Giddings, B.W., Brooks, M.W., Buday, L., Sizeland, A.M., and Weinberg, R.A. (1993). Association of Sos Ras exchange protein with Grb2 is implicated in tyrosine kinase signal transduction and transformation. *Nature* 363, 45–51.
- Ferguson, K.M., Kavran, J.M., Sankaran, V.G., Fournier, E., Isakoff, S.J., Skolnik, E.Y., and Lemmon, M.A. (2000). Structural basis for discrimination of 3-phosphoinositides by pleckstrin homology domains. *Mol. Cell* 6, 373–384.
- Gale, N.W., Kaplan, S., Lowenstein, E.J., Schlessinger, J., and Bar-Sagi, D. (1993). Grb2 mediates the EGF-dependent activation of guanine nucleotide exchange on Ras. *Nature* 363, 88–92.
- Hall, B.E., Yang, S.S., Boriack-Sjodin, P.A., Kuriyan, J., and Bar-Sagi, D. (2001). Structure-based mutagenesis reveals distinct functions for Ras switch 1 and switch 2 in Sos-catalyzed guanine nucleotide exchange. *J. Biol. Chem.* 276, 27629–27637.
- Hall, B.E., Yang, S.S., and Bar-Sagi, D. (2002). Autoinhibition of Sos by intramolecular interactions. *Front. Biosci.* 7, d288–d294.
- Hanzal-Bayer, M., Renault, L., Roversi, P., Wittinghofer, A., and Hillig, R.C. (2002). The complex of Arl2-GTP and PDE delta: from structure to function. *EMBO J.* 21, 2095–2106.
- Kim, J.H., Shirouzu, M., Kataoka, T., Bowtell, D., and Yokoyama, S. (1998). Activation of Ras and its downstream extracellular signal-regulated protein kinases by the CDC25 homology domain of mouse Son-of-sevenless 1 (mSos1). *Oncogene* 16, 2597–2607.
- Kleywegt, G.J., and Jones, T.A. (1996). Efficient rebuilding of protein structures. *Acta Crystallogr. D Biol. Crystallogr.* 52, 829–832.
- Kraemer, A., Brinkmann, T., Plettner, I., Goody, R., and Wittinghofer, A. (2002). Fluorescently labelled guanine nucleotide binding proteins to analyse elementary steps of GAP-catalysed reactions. *J. Mol. Biol.* 324, 763–774.
- Li, N., Batzer, A., Daly, R., Yajnik, V., Skolnik, E., Chardin, P., Bar-Sagi, D., Margolis, B., and Schlessinger, J. (1993). Guanine-nucleotide-releasing factor hSos1 binds to Grb2 and links receptor tyrosine kinases to Ras signalling. *Nature* 363, 85–88.
- Margarit, S.M., Sondermann, H., Hall, B.E., Nagar, B., Hoelz, A., Pirruccello, M., Bar-Sagi, D., and Kuriyan, J. (2003). Structural evidence for feedback activation by Ras.GTP of the Ras-specific nucleotide exchange factor SOS. *Cell* 112, 685–695.
- Milburn, M.V., Tong, L., deVos, A.M., Brünger, A., Yamaizumi, Z., Nishimura, S., and Kim, S.H. (1990). Molecular switch for signal transduction: structural differences between active and inactive forms of protooncogenic ras proteins. *Science* 247, 939–945.
- Nimnual, A., and Bar-Sagi, D. (2002). The two hats of SOS. *Sci STKE* 2002, PE36. 10.1126/stke.2002.145.pe36
- Nimnual, A.S., Yatsula, B.A., and Bar-Sagi, D. (1998). Coupling of Ras and Rac guanosine triphosphatases through the Ras exchanger Sos. *Science* 279, 560–563.
- Otwinowski, Z., and Minor, W. (1997). Processing of X-ray diffraction data collected in oscillation mode. *Methods Enzymol.* 276, 307–326.
- Pai, E.F., Krenkel, U., Petsko, G.A., Goody, R.S., Kabsch, W., and Wittinghofer, A. (1990). Refined crystal structure of the triphosphate conformation of H-ras p21 at 1.35 Å resolution: implications for the mechanism of GTP hydrolysis. *EMBO J.* 9, 2351–2359.
- Qian, X., Vass, W.C., Papageorge, A.G., Anborgh, P.H., and Lowy, D.R. (1998). N terminus of Sos1 Ras exchange factor: critical roles for the Dbl and pleckstrin homology domains. *Mol. Cell. Biol.* 18, 771–778.
- Silver, S.J., Chen, F., Doyon, L., Zink, A.W., and Rebay, I. (2004). New class of Son-of-sevenless (Sos) alleles highlights the complexities of Sos function. *Genesis* 39, 263–272.
- Sini, P., Cannas, A., Koleske, A.J., Di Fiore, P.P., and Scita, G. (2004). Abl-dependent tyrosine phosphorylation of Sos-1 mediates growth-factor-induced Rac activation. *Nat. Cell Biol.* 6, 268–274.
- Soisson, S.M., Nimnual, A.S., Uy, M., Bar-Sagi, D., and Kuriyan, J.

(1998). Crystal structure of the Dbl and pleckstrin homology domains from the human Son of sevenless protein. *Cell* 95, 259–268.

Sondermann, H., Soisson, S.M., Bar-Sagi, D., and Kuriyan, J. (2003). Tandem histone folds in the structure of the N-terminal segment of the ras activator Son of Sevenless. *Structure* 11, 1583–1593.

Vetter, I.R., and Wittinghofer, A. (2001). The guanine nucleotide-binding switch in three dimensions. *Science* 294, 1299–1304.

Worthylake, D.K., Rossman, K.L., and Sondek, J. (2000). Crystal structure of Rac1 in complex with the guanine nucleotide exchange region of Tiam1. *Nature* 408, 682–688.

Yarden, Y., and Sliwkowski, M.X. (2001). Untangling the ErbB signalling network. *Nat. Rev. Mol. Cell Biol.* 2, 127–137.

Accession Numbers

Crystallographic coordinates and structure factors have been deposited in the Protein Data Bank under accession codes 1XD2, 1XD4, and 1XDV.

**This Page is Inserted by IFW Indexing and Scanning
Operations and is not part of the Official Record**

BEST AVAILABLE IMAGES

Defective images within this document are accurate representations of the original documents submitted by the applicant.

Defects in the images include but are not limited to the items checked:

- ☒ BLACK BORDERS
- ☒ IMAGE CUT OFF AT TOP, BOTTOM OR SIDES
- ☒ FADED TEXT OR DRAWING
- ☒ BLURRED OR ILLEGIBLE TEXT OR DRAWING
- ☐ SKEWED/SLANTED IMAGES
- ☐ COLOR OR BLACK AND WHITE PHOTOGRAPHS
- ☐ GRAY SCALE DOCUMENTS
- ☐ LINES OR MARKS ON ORIGINAL DOCUMENT
- ☐ REFERENCE(S) OR EXHIBIT(S) SUBMITTED ARE POOR QUALITY
- ☐ OTHER: _____

IMAGES ARE BEST AVAILABLE COPY.

As rescanning these documents will not correct the image problems checked, please do not report these problems to the IFW Image Problem Mailbox.